Luis Manuel Canonico Armas

Revisiting the Quantum Hall effect in the Haldane Model

Niterói, 2017

Universidade Federal Fluminense

Instituto de Física da Universidade Federal Fluminense

Luis Manuel Canonico Armas

Revisiting the Quantum Hall effect in the Haldane Model

Orientador: Prof. Dr. Roberto Bechara Muniz

Coorientadora: Profa. Dra. Tatiana G. Rappoport

Dissertação de mestrado apresentada ao Instituto de Física da Universidade Federal Fluminense para obtenção do título de Mestre em Física

Este exemplar corresponde à versão final da dissertação defendida pelo aluno Luis Manuel Canonico Armas, e orientada pelo Prof. Dr. Roberto Bechara Muniz.

Niterói, 2017

DEDICATORY

To my family, to my friends
and those who have contributed in this journey.

ACKNOWLEDGMENT

"Always Pass on,
What You Have Learned."
— Yoda

RESUMO

O modelo de Haldane numa rede honeycomb é um dos exemplos mais simples de sistemas que apresentam condutividade Hall quantizada na ausência de campos magnéticos aplicados - também conhecido como efeito Hall quântico anômalo. Utilizando cálculos analíticos e numéricos, nós mostramos que esse modelo possui espectros de energia distintos na presença de campos magnéticos externos de mesma intensidade, porém com sentidos opostos. Essas diferenças vinham sendo ignoradas em cálculos anteriores e mostram que aproximações de baixas energias não são sempre apropriadas para estudar propriedades eletrônicas desse sistema.

Palavras-chave: Haldane model, Tight Binding, Kernel Polynomial Method, Chern Insulators

ABSTRACT

The Haldane model in a honeycomb lattice is one of the simplest examples of systems that present a quantized Hall conductivity in the absence of an external magnetic field - also known as quantum anomalous Hall effect. By means of analytical and numerical calculations, we show that this model presents different energy spectrum and Hall conductivity in the presence of positive and negative external magnetic fields of same intensity. This difference was ignored by previous calculations and indicates that the low-energy approximation is not always sufficient to capture important features of the electronic properties described by tight-binding Hamiltonians.

Keywords: Haldane model, Tight Binding, Kernel Polynomial Method, Chern Insulators

CONTENTS

1

INTRODUCTION

More than a century ago, Edwin Hall discovered the Hall effect [1]. It consists in the appearance of a transverse voltage difference across a conducting material when an electric current flows through the system in the presence of a perpendicular applied magnetic field, as illustrated in fig. 1 (a). One year after his discovery, Edwin Hall also measured the Hall voltage in paramagnetic metals and found that it was often much larger than in ordinary metals; this new effect depends on the magnetization of the system, is also present in ferromagnetic materials, and is called anomalous Hall effect (see fig 1 (b)).

Over a century after the discovery of the Hall effect, the first sights of its quantum version were reported by K. von Klitzing *et al.* [2]. In their work, they performed careful measurements of the Hall resistivity in MOSFET transistors at very low temperatures and high magnetic fields (quantum limit), and observed that the Hall conductivity of a two dimensional electron gas in the inversion layer of the transistor takes quantized values of $\frac{e^2}{h}$ (see Fig. 1 (d)).
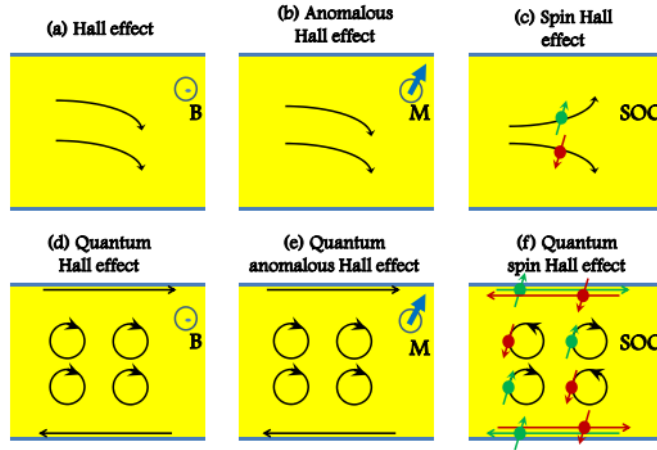
Figure 1: Illustration of different types of Hall effect (figure taken from Ref. [3])

The discovery of the quantum Hall effect motivated subsequent experimental works, aiming to find if this new phenomenon depended on both the geometry of the sample and concentration of impurities. An important result of these experiments is that the integer values of the quantized Hall conductivity are well defined independently of the geometry of the system, and in a certain range of disorder [4].

Among the experimental studies of the quantum Hall effect, there was another important experiment carried out by Tsui *et al.* [5], where using high mobility samples detected that the plateaus of the conductivity can acquire multiple fractional values of $\frac{e^2}{h}$. As the amount of disorder is decreased, the plateaus of the Hall resistivity at integer values become less prominent, but other plateaus emerge at fractional values. Beside the existence of the fractional quantum Hall effect, which is due to electron-electron interactions, the results of Tsui *et al.* confirms the idea that the robustness of the Hall conductivity values (both integer and fractional) should be related to a fundamental principle.

The early experimental data on the quantization of the Hall effect not only motivated further experimental works, but also a considerable amount of theoretical investigations aiming to understand this phenomenon. The first theoretical explanation of the integer

quantum Hall effect was provided by a thought experiment devised by R. Laughlin [6], which was later extended by B. I. Halperin [7]. To formulate his argument, Laughlin considered a system with the geometry shown in figure 2. He assumed that the system had some impurities to broaden the Landau levels, forming bands of extended states separated by tails of localized states which do not contribute to the Hall conductivity.

The applied magnetic field sketched in figure 2, has a vector potential $\vec{A}$ that modifies the phase of the wave-functions. Hence, changes in the applied field will produce a gauge transformation of each wave function of the system. However, to preserve the coherence of these functions through the loop, these changes on the magnitude of the potential vector have to be restricted. As a consequence of the limitation of the possible values of the vector potential, when we pass a quantum of magnetic flux through the system, the Hamiltonian for this case is mapped to the initial one (see figure 2).

The increment of the field is treated as an adiabatic cycle, and its total effect is the transfer of charge from one edge of the ribbon to the other. These charges contribute to the formation of the Hall potential. Nevertheless, due the existence of the localized states, some of the charges can be hosted by these states, and this explained the existence of the constant plateaus in the transverse conductivity.
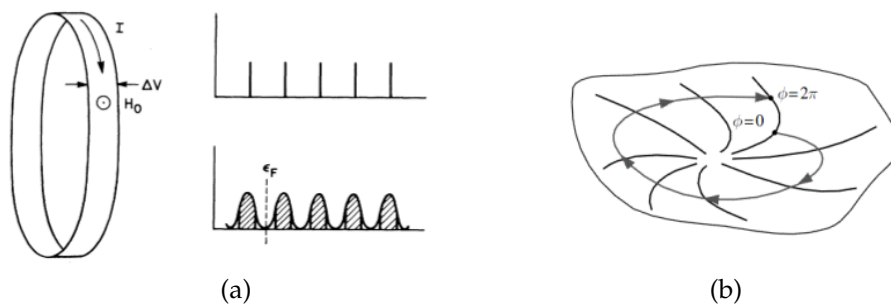
Figure 2: (a) Ideal model proposed by Laughlin. (b) Diagrammatic representation of the spectral flow of the Hamiltonian in the space of parameters.

Although the ingenious though experiment proposed by Laughlin managed to explain the exactness of the quantization of the Hall effect, a deeper understanding of the Hall effect in crystalline materials was needed. If Laughlin's thought experiment is applied in such a naive way, this can lead to paradoxes. To solve these problems, Thouless *et al.* derived a new formula to calculate the Hall conductivity σ_H, during the study of the Hall conductivity in a 2 dimensional system of electrons in presence of a periodic potential. This new formula was derived from the Kubo formula, is completely general [8] and depends solely on the properties of the wave functions of the system.

A year later, M. V. Berry discovered the existence of a geometric phase in adiabatic quantum mechanics [9]. In the very same year, B. Simon published a work connecting the results obtained by M. V. Berry and Thouless *et al.* [10]. In his article, Simon recognized the Thouless-Kohmoto-Nightingale-den Nijs (TKNN) invariant as the integral of the curvature associated with a Berry phase in the Brillouin zone. The importance of the paper of Thouless *et al.* is that it provides a general and concrete explanation of the quantum Hall effect and also opens the possibility of having Hall conductance in absence of external magnetic fields (anomalous quantum Hall effect) [11].

Following the results of the works of Thouless *et al.* [10, 11], six years later D. Haldane took the next conceptual step on the study of the Hall conductance [12]. He proved that to produce a quantum Hall state, there must exist a time-reversal symmetry breaking, which in the previous works had been caused by an external magnetic field. In his work, Haldane took the tight-binding Hamiltonian of "2*D* graphite" (graphene) previously investigated by Semenoff [13] and added a complex second nearest-neighbors term which works as a local magnetic field with zero magnetic flux through the unit cell, in order to break mathematically the time-reversal symmetry.

The non-trivial topological phase and the gapped state in the Haldane model defined a new phase of the matter which is now called Chern insulators [14]. The experimental observations of the so called quantum anomalous Hall effect (QAHE) at zero magnetic

field in novel materials happened twenty five years after the publication of Haldane. The QAHE was detected in *Cr*-doped $Bi(Sb)_2Te_3$ films[15]. After these results, more experimental studies of the Hall conductivity in Chern insulators were performed [16, 17], but three years ago there was also a novel application using cold atoms techniques: the Haldane model was realized in optical lattices [18].

The later theoretical and experimental findings make clear that the Haldane model is an useful tool to study the topological phases of the matter. This model also served as the cornerstone to study the spin quantum Hall effect, which was proposed initially by Kane and Mele by adding a spin degree of freedom to the spinless system of the Haldane model [19]. Further properties of the matter can be described with this model, but when a high degree of disorder is considered, the approximative analytical calculations become inviable. To study disordered systems one should recur to the numerical methods.

Distinct numerical methods may be used to calculate the electronic properties of different systems, but when translational symmetry is broken (as in disordered systems), the best approach is to work in real space. Non-interacting electronic properties of finite systems with D lattice sites are described by a $D \times D$ Hamiltonian matrix, and may be obtained either from its diagonalization, or by a matrix inversion to get the one-electron Green's functions. This approach has a downside, because to achieve a good description of bulk systems one should try to reach the thermodynamic limit $D \to \infty$ [20]. However, the computational effort required to calculate the eigenvalues through exact diagonalization usually scales rapidly (with D^3), making this approach intractable for very large systems [21].

An alternative to those exact methods are the $\mathcal{O} - D$ algorithms, where the computational effort scales linearly with the size of the system. In these methods, the spectral functions are expanded in a base of polynomials and the focus of the computational effort goes to the calculation of the expansion moments. The major drawback of these

methods is the error induced by the truncation of the series, which leads to the so called Gibbs oscillations [21].

The Gibbs oscillations can be controlled by introducing a damping factor, known as kernel, in the series representation. It smooths the represented functions, eliminate the Gibbs oscillations and increases the series convergence [22, 23, 24]. There exist a diversity of kernels for different sets of polynomials. Chebyshev polynomials are one of the most used sets, due to their trigonometric representation, fast convergence rate (in comparison with other polynomial bases) and their recurrence relation, which is useful for iterative schemes. In the early 90s Silver *et al.* used the Chebyshev expansion to approximate the spectral properties of tight-binding Hamiltonians [23, 24]. They considered a set of kernels in their study, finding that the optimal kernel known as the Jackson kernel minimizes the Gibbs oscillations and improves the resolution. The combination of this kernel and Chebyshev polynomials today is known as the kernel polynomial method (KPM). The main advantage of this method is that the computational cost scales linearly with the size of the system, making the numerical study of larger systems accessible [23, 24, 21].

In this thesis, we extend the study of the effect of external magnetic fields in the Haldane model, performed by X.Y. Wang *et al* [25]. Instead of using the Kubo formula with the Fukui algorithm [26], we apply the kernel polynomial method with a novel method developed by J. Garcia *et al.* [27, 28] to calculate the Hall conductivity. We show numerically that in the limit of high magnetic fields, the symmetry of the spectrum between positive and negative fields is broken. The positive and negative spectra have a shift that depends upon the sign of the field, which has been ignored in the original work of Haldane and subsequent analyses. We present our numerical calculations of the Hall conductivity for opposite fields, where magnetic oscillations in the anomalous contribution of the conductivity are found. We also study the low-energy expansion of the Haldane model, and extend it to obtain an analytical expression for the shift in the spectrum, in order to explain the existence of magnetic oscillations in the anomalous

part of the Hall conductivity.

This thesis is organized as follows: In chapter 2, we present a tight-binding description of the Haldane model. We begin with a brief revision of the basic structural properties of the honeycomb lattice, then we calculate the eigenvalues of the Haldane model, and by performing a Taylor series expansion near of the Dirac points we review the low-energy limit of the spectrum. We classify the topological phases of this model according to the possible values of the Chern numbers, and we include the effect of the external magnetic fields in the tight-binding Hamiltonian using the Peierls' phase. We also give a short introduction to the Kernel Polynomial Method and highlight some of the properties of the Chebyshev polynomials. We discuss the errors induced by the truncation of the Chebyshev series and how the kernels improve its convergence. At the end of chapter 2, we present the results of the numerical calculations of the density of states of the Haldane model with external magnetic fields in two different limits: the case without second nearest-neighbors hopping (graphene) and the case of pure imaginary hopping. We show that field inversion symmetry is not preserved in this model.

In chapter 3, we review the low-energy continuum model to identify the origin of the difference in the spectrum of positive and negative fields. We begin by revising the low-energy model at zeroth order of the Taylor series expansion of the Haldane term near the Dirac point. We use the Landau-Peierls substitution together with Landau quantization, to obtain the energy spectrum. We then consider higher order in the Haldane term expansion in the vicinity of the Dirac points, to find that the energy spectrum shifts by a constant that depends on the field's sign. With the corrected expression for the eigenvalues and the new Hamiltonian, we calculate the Hall conductivity with the Kubo formula. We present a classification of the transitions that contribute to the Hall conductivity, and managed to show that the continuum model with the second order corrections reproduces the oscillations numerically obtained for the anomalous Hall

conductivity.

Finally in chapter 4, we compare our numerical and analytical results. We discuss the limits where the low-energy approximation corresponds the numerical results, and what parameters modify the correspondence between the low-energy approximation and the numerical results.

2 | HALDANE MODEL:TIGHT BINDING APPROACH

2.1 INTRODUCTION

The Haldane model is the simplest realization of a Chern insulator in a honeycomb lattice [12]. The importance of this model resides on the fact that it exhibits quantum Hall effect in the absence of external magnetic fields. It was proposed by Haldane in 1988 as a basic theoretical representation for the quantum anomalous Hall effect.

This model represented a remarkable turnaround, because until its formulation, the quantum Hall effect in two dimensional materials was associated with the presence of external magnetic fields [1, 2, 6]. Following the results of Thouless *et al.* [8, 11], Haldane proved that the existence of a quantum Hall state does not strictly depend upon the presence of external magnetic fields, but on the symmetries of the system and its topological phases [8, 14].

In this chapter, we revise the most important properties of the Haldane model. We calculate its eigenvalues and discuss its topological properties. We also implement the Peierls substitution to include the electron interaction with external magnetic fields in the tight-binding Hamiltonian. To improve the conception of our numerical analysis, we briefly revise the Kernel Polynomial Method, and show our results of the density of states and Hall conductivity calculated for the Haldane model in the presence of an external magnetic field.

2.2 LATTICE VECTORS

We begin with a brief revision of the structural properties of the honeycomb lattice. It is widely known that the honeycomb lattice despite having hexagonal form is not an hexagonal lattice; its structure consists of the interpenetration of two triangular lattices. An effective way to describe this lattice is to think of it as a triangular lattice with a basis consisting of two atoms, each belonging to a different sub-lattice. This point of view enables us to construct mathematically a sheet of honeycomb-arranged sites from two primitive vectors. The set of primitive vectors with lattice constant a that we use are:

$$\vec{a_1} = \left(\sqrt{3}a, 0\right), \quad \vec{a_2} = \left(\frac{\sqrt{3}a}{2}, \frac{3a}{2}\right). \tag{1}$$

Beside the vectors in (1), to fully describe the lattice, we must specify how a crystal site is connected to its nearest neighbors. For that, we can use the vectorial quantities:

$$\vec{e_1} = (0, a), \quad \vec{e_2} = \left(-\frac{\sqrt{3}}{2}, -\frac{a}{2}\right), \quad \vec{e_3} = \left(\frac{\sqrt{3}}{2}, -\frac{a}{2}\right). \tag{2}$$

With the primitive vectors of the lattice and the vectors that indicate how a crystal site is connected with its nearest neighbors, we have the minimum requirements to describe the honeycomb lattice. However, to implement the Haldane model [12] we need to specify also the next-nearest neighbors in the crystal, that are given by

$$\vec{v_1} = \left(\sqrt{3}a, 0\right), \quad \vec{v_2} = \left(\frac{-\sqrt{3}}{2}a, \frac{3}{2}a\right), \quad \vec{v_3} = \left(-\frac{\sqrt{3}}{2}a, -\frac{3}{2}a\right). \tag{3}$$

In figure 3 we show the primitive vectors of the lattice, the nearest neighbor and the next-nearest neighbors of the crystal in panels (a), (b) and (c) respectively. Once defined the vectorial quantities that describe the honeycomb lattice and the vectors that relate a lattice site with its next-nearest neighbors, we are ready to calculate the eigenvalues of the Haldane model.
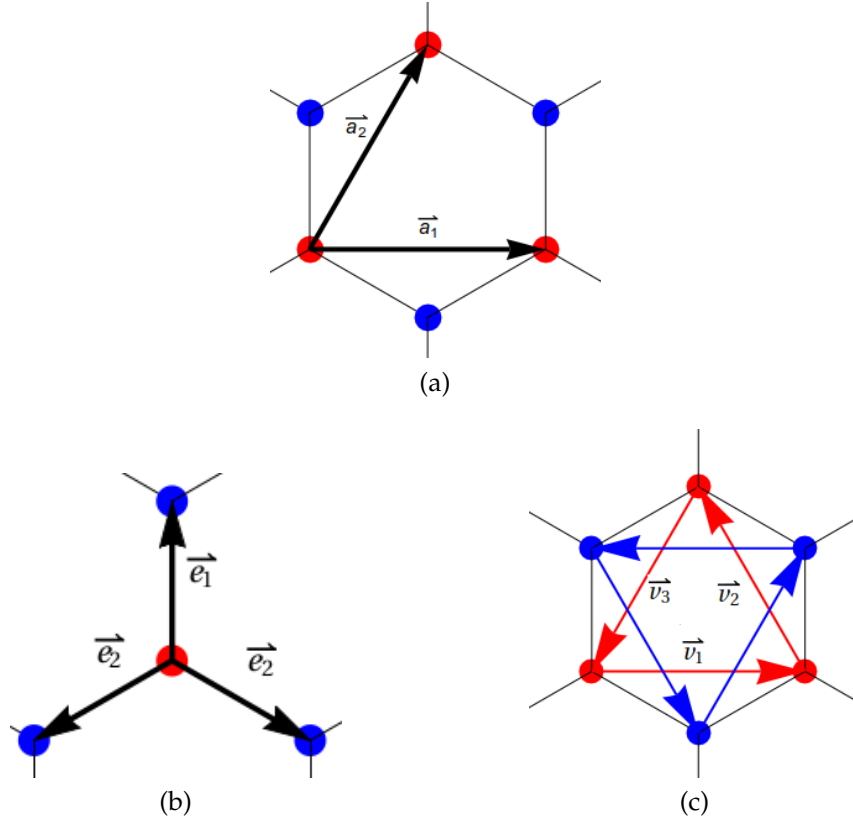
Figure 3: Lattice vectors of the honeycomb lattice: Primitive vectors (a). Nearest neighbors (b). Next-nearest neighbors (c).

2.3 EIGENVALUES OF THE HALDANE MODEL

In the previous section, we have presented the structural properties of the honeycomb lattice that is used in our study. This section is focused on the calculation of the eigenvalues of the Haldane model in absence of external magnetic fields and on discussions of some of its properties. As stated previously, this model was devised by Haldane to illustrate the materialization of the quantum Hall effect in a honeycomb lattice without external magnetic fields[12]. To achieve this, Haldane added two terms to the single-orbital tight binding Hamiltonian that describes the electronic structure of graphene [29, 30]. The first term describes second nearest-neighbor hoppings that are complex. The signs of the arguments of the associated hopping integrals depend upon

the hopping directions and, as a consequence, this term breaks time-reversal symmetry. The second term introduces an on-site potential energy that breaks inversion symmetry between the two sub-lattices. The Hamiltonian that characterizes the Haldane model is given by

$$
H = \left[-t \sum_{\langle i,j \rangle} a_i^\dagger b_j + \frac{M}{2} \sum_{i=1} \left(a_i^{\dagger} a_i - b_i^{\dagger} b_i \right) \right] + h.c + t_2 \sum_{\langle\langle i,j \rangle\rangle} e^{i\varphi} a_i^\dagger a_j + t_2 \sum_{\langle\langle i,j \rangle\rangle} e^{-i\varphi} b_i^\dagger b_j. \quad (4)
$$

Here t and t_2 are the amplitudes of the nearest and the next-nearest neighbor hopping integrals, respectively; $a_i^\dagger$ and a_i designate the creation and annihilation operators for electrons on sites i and j, respectively, both belonging to one of the sub-lattices. Similarly, $b_i^\dagger$ and b_j represent the creation and annihilation operators for electrons on sites i and j, respectively, both belonging to the other sub-lattice. $\langle i,j \rangle$, and $\langle\langle i,j \rangle\rangle$ indicate that the sums are restricted to the first and second nearest neighbors sites only, respectively; φ is the phase of t_2 (this is equivalent to a Peierls phase with zero total flux per unit cell), and M is an on-site energy. We notice that the last term in Eq. (4) leads to a gap of size $2M$ in the electronic structure described by H, when t_2 is absent.

To obtain the eigenvalues of this model, we can write the Hamiltonian (4) in the momentum space. Performing a Fourier transformation [29] in Hamiltonian (4), we obtain:

$$
H = \sum_k \left(a_k^{\dagger} \ b_k^{\dagger} \right) \begin{pmatrix} \mathcal{H}_{11} & \mathcal{H}_{12} \\ \mathcal{H}_{21} & \mathcal{H}_{22} \end{pmatrix} \begin{pmatrix} a_k \\ b_k \end{pmatrix} \quad (5)
$$

From (5), we identify that the properties of the Hamiltonian are contained in:

$$
\mathcal{H} = \begin{pmatrix} \mathcal{H}_{11} & \mathcal{H}_{12} \\ \mathcal{H}_{21} & \mathcal{H}_{22} \end{pmatrix} , \quad (6)
$$

where the factors $\mathcal{H}_{ij}$ $(i, j = 1, 2)$ are:

$$\mathcal{H}_{12} = -t \sum_{i=1}^{3} e^{-i\vec{k} \cdot \vec{e}_i} \qquad\qquad \mathcal{H}_{21} = -t \sum_{i=1}^{3} e^{i\vec{k} \cdot \vec{e}_i},$$

$$\mathcal{H}_{11} = -2t_2 \sum_{i=1}^{3} \left[\cos\left(\vec{k} \cdot \vec{v}_i - \varphi\right)\right] + M \qquad \mathcal{H}_{22} = -2t_2 \sum_{i=1}^{3} \left[\cos\left(\vec{k} \cdot \vec{v}_i + \varphi\right)\right] - M.$$

$$(7)$$

To obtain a simple expression for the eigenvalues of the system, we may use the Pauli matrices to rewrite the Hamiltonian (6) as:

$$\mathcal{H} = \mathcal{H}_0 I + \mathcal{H}_x \sigma_x + \mathcal{H}_y \sigma_y + \mathcal{H}_z \sigma_z \quad , \tag{8}$$

where the factors $\mathcal{H}_i$ $(i = 0, x, y, z)$ are:

$$\mathcal{H}_0 = \frac{1}{2}\left(\mathcal{H}_{11} + \mathcal{H}_{22}\right) = -2t_2 \cos(\varphi) \sum_{i=1}^{3} \left[\cos\left(\vec{k} \cdot \vec{v}_i\right)\right],$$

$$\mathcal{H}_z = \frac{1}{2}\left(\mathcal{H}_{11} - \mathcal{H}_{22}\right) = M - 2t_2 \sin(\varphi) \sum_{i=1}^{3} \left[\sin\left(\vec{k} \cdot \vec{v}_i\right)\right],$$

$$\mathcal{H}_x = \Re\left[\mathcal{H}_{21}\right] = -t \sum_{i=1}^{3} \left[\cos\left(\vec{k} \cdot \vec{e}_i\right)\right],$$

$$\mathcal{H}_y = \Im\left[\mathcal{H}_{21}\right] = -t \sum_{i=1}^{3} \left[\sin\left(\vec{k} \cdot \vec{e}_i\right)\right]. \tag{9}$$

Note that if we set the value of $t_2 = 0$ and $M = 0$ in (9), the Hamiltonian (8) is the tight-binding Hamiltonian that describes pristine graphene. Diagonalizing (8), we obtain the eigenvalues of the Haldane model:

$$\epsilon_{\pm}(\vec{k}) = \mathcal{H}_0\left(\vec{k}\right) \pm \sqrt{\mathcal{H}_x\left(\vec{k}\right)^2 + \mathcal{H}_y\left(\vec{k}\right)^2 + \mathcal{H}_z\left(\vec{k}\right)^2}. \tag{10}$$

In figure 4 we show a plot of the band structure of the Haldane model. In this figure, the author varies different parameters in the Hamiltonian to see how the energy band changes. Panel (a) represents the situation where next-nearest neighbor hopping are zero (graphene). Panel (b) shows the bandstructure for $t_2 \neq 0$ and $M = 0$, where we can see the opening of a gap in the Dirac points caused by the hopping that connects the next-nearest neighbors. Panels (c) and (d) depict the cases where the inter-lattice potential has the same magnitude of the second hopping terms in $\mathcal{H}_z$, which results in the closure of the gap in one of the Dirac points.
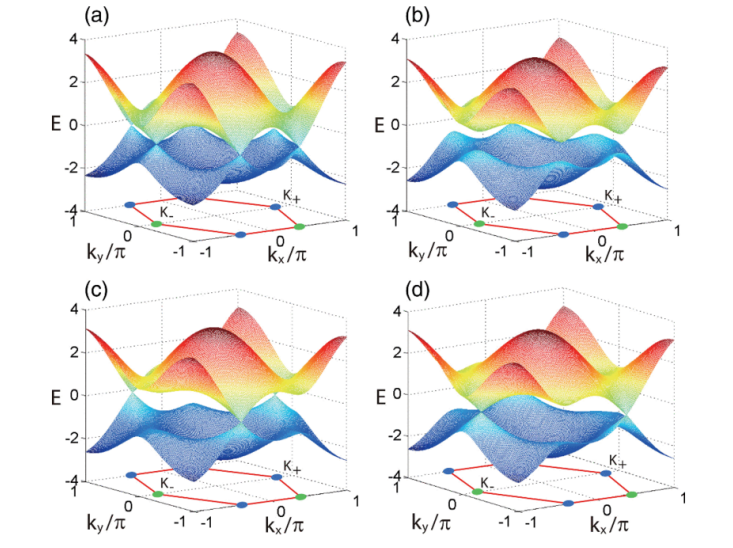

Figure 4: Band structure of the Haldane model with $t = 1$ and $t_2 = 0.1$. (a) $M = 0$ and $\varphi = 0$; (b) $M = 0$ and $\varphi = \frac{\pi}{3}$; (c) $M = 3\sqrt{3}t_2 \sin(\varphi)$ and $\varphi = \frac{\pi}{3}$; (d) $M = -3\sqrt{3}t_2 \sin(\varphi)$ and $\varphi = \frac{\pi}{3}$. Figure taken from reference [31]

2.4 TOPOLOGY IN THE HALDANE MODEL

Thouless *et al.* proved that the existence of a non-zero value of the quantum Hall conductivity depends on the properties of the wave functions [8]. Along the same line Kohmoto showed that the impossibility to define an unique and smooth wave function for the system in the whole Brillouin zone is related to the existence of non-trivial topologies, which are responsible for non-zero quantum Hall effect values [32]. To illustrate the topological properties of the Haldane Model, we consider the low-energy limit of this model to obtain the wave functions and study their singularity points.

To obtain the low-energy Hamiltonian, we have performed a Taylor expansion of the Hamiltonian (8) about the Dirac points. Substituting the explicit expressions for $\mathcal{H}_0$, $\mathcal{H}_x$, $\mathcal{H}_y$ and $\mathcal{H}_z$ in (10), and expanding them in the vicinity of the Dirac points we obtain:

$$H(\vec{k}) = \begin{pmatrix} m_\tau & v_F(\hbar\tau k_x - i\hbar k_y) \\ v_F(\hbar\tau k_x + i\hbar k_y) & -m_\tau \end{pmatrix} \, , \tag{11}$$

with eigenvalues

$$\epsilon_\pm(\vec{k}) = \pm\sqrt{\left(\hbar v_F \vec{k}\right)^2 + m_\tau^2} = \pm|\epsilon(\vec{k})|, \tag{12}$$

where τ represents the choice of the Dirac point; for the point $\vec{K} = \left[\dfrac{4\pi}{3\sqrt{3}a}, 0\right]$, we set $\tau = 1$, and for the point $\vec{K}' = \left[\dfrac{-4\pi}{3\sqrt{3}a}, 0\right]$, we chose $\tau = -1$. Here, $v_F = \frac{3ta}{2\hbar}$ represents the Fermi velocity, and the factor $m_\tau = M - 3\sqrt{3}\tau t_2 \sin(\varphi)$ is the zeroth order expansion of the second term added by Haldane and contents the information related to the next nearest neighbor hopping. In (12) we have omitted the expansion of $\mathcal{H}_0$ near of the Dirac point because it is a constant that does not affect the relative distance between the bands.

The eigenfunction associated with $\epsilon_-(\vec{k}) = -|\epsilon(\vec{k})|$ is given by:

$$\psi^{(I)}(\vec{k}) = \frac{1}{\sqrt{2\left(|\epsilon(\vec{k})|^2 - |\epsilon(\vec{k})|m_\tau\right)}} \begin{pmatrix} m_\tau - |\epsilon(\vec{k})| \\ \hbar v_F \left(\tau k_x + i k_y\right) \end{pmatrix}. \tag{13}$$

Examining equation (13), it is clear that the eigenfunction evaluated at the Dirac point $\vec{K}$ ($\tau = 1$) does not become singular unless $M > 3\sqrt{3}t_2 \sin(\varphi)$. However, let us investigate the behavior of this function in the vicinity of $\vec{K}'$ ($\tau = -1$). To check it, we set $\vec{k} = 0$ and $\tau = -1$ in (13) to obtain:

$$\psi^{(I)}(0) = \frac{1}{\sqrt{2\left(|\epsilon(0)|^2 - |\epsilon(0)|m_-\right)}} \begin{pmatrix} m_- - |\epsilon(0)| \\ 0 \end{pmatrix}, \tag{14}$$

where $\epsilon_-(\vec{0}) = -|m_-|$ is the energy of the band in the Dirac point and $m_- = M + 3\sqrt{3}t_2 \sin(\varphi)$.

From (14) it is clear that the eigenfunction (13) evaluated in $\vec{K}'$ turns out to be singular unless $M < -3\sqrt{3}t_2 \sin(\varphi)$. The impossibility to define the wave function for the whole Brillouin zone when $-3\sqrt{3}t_2 \sin(\varphi) < M < 3\sqrt{3}t_2 \sin(\varphi)$ force us to redefine this function in order to describe the $\vec{K}'$ point. To redefine the wave function at $\vec{K}'$, we follow the method devised by Kohmoto. The freedom of choosing the phase of the wave function, enables us to use a gauge transformation of the kind

$$u_{\vec{k}}(x, y) \rightarrow u_{\vec{k}}(x, y) e^{if(\vec{k})}, \tag{15}$$

where $u_{\vec{k}}(x, y)$ represents the periodic part of the Bloch waves and $f(\vec{k})$ is an smooth function of $\vec{k}$. This transformations does not change the eigenvalues, but allow us to avoid the singularity. The redefinition of the wave function in the vicinity of $\vec{K}'$ suggests a separation of the Brillouin zone in two sectors. The first (named $H^{(I)}$) contains the $\vec{K}$ points, where $\psi^{(I)}$ is defined, while the second (called $H^{(II)}$) contains the $\vec{K}'$ points

where $\psi^{(I)}$ becomes singular. Using the transformation (15), the new wave function is written as:

$$
\psi^{(II)} = \psi^{(I)} \times e^{i\phi(\vec{k})} = \frac{1}{\sqrt{2\left(|\epsilon(\vec{0})|^2 + |\epsilon(\vec{0})|m_\tau\right)}} \begin{pmatrix} -\hbar v_F\left(\tau k_x - ik_y\right) \\ m_\tau + |\epsilon(\vec{0})|, \end{pmatrix} , \qquad (16)
$$

where the phase factor is defined as:

$$
e^{i\phi(\vec{k})} = \left[\frac{m_\tau + |\epsilon(0)|}{|m_\tau + |\epsilon(0)||}\right]\left[\frac{|\hbar v_F\left(\tau k_x + ik_y\right)|}{\hbar v_F\left(\tau k_x + ik_y\right)}\right] \qquad (17)
$$

To calculate the Hall conductivity, we use the expression

$$
\sigma_{xy} = \frac{e^2}{h}\frac{1}{2\pi i}\int d^2k \int d^2r \left(\frac{\partial u_{\vec{k}}^*}{\partial k_y}\frac{\partial u_{\vec{k}}}{\partial k_x} - \frac{\partial u_{\vec{k}}^*}{\partial k_x}\frac{\partial u_{\vec{k}}}{\partial k_y}\right) \qquad (18)
$$

obtained by Thouless *et al.* using the Kubo formula to calculate the transverse Hall conductivity. The equation (18) is known as the TKNN invariant of first form; regrouping the factors in this equation, the Hall conductivity can be expressed as:

$$
\sigma_{xy} = \frac{e^2}{h}\frac{1}{2\pi i}\int_{BZ} d^2k \left[\vec{\nabla}_k \times \vec{A}(\vec{k})\right]_z = \frac{e^2}{h}\frac{1}{2\pi i}\int_{BZ} d^2k\, \Omega_{\vec{k}}, \qquad (19)
$$

in which the Berry vector potential $\vec{A}(\vec{k})$ is defined as

$$
\vec{A}(\vec{k}) = \int d^2r\, u_{\vec{k}}^*\vec{\nabla}_k u_{\vec{k}} = \langle u_{\vec{k}}|\vec{\nabla}_k|u_{\vec{k}}\rangle. \qquad (20)
$$

The equation (19) is known as the TKNN invariant of second form [32]. The equations (18) and (19) have as a result an integer number which is called Chern number, which is the integration of the Berry curvature $\Omega_{\vec{k}}$ in the whole Brillouin zone and gives the magnitude of the plateaus in the transverse conductivity. Since we have chosen a distinct wave function in each Brillouin zone sector, one finds two Berry vector potentials $\vec{A}^{(I)}$ and $\vec{A}^{(II)}$ associated with them. They are connected by the relation:

$$
\vec{A}^{(II)}(\vec{k}) = \vec{A}^{(I)}(\vec{k}) + i\nabla_k f(\vec{k}). \qquad (21)
$$

As a result, Eq. (19) may be rewritten as:

$$\sigma_{xy} = \frac{e^2}{h} \frac{1}{2\pi i} \left[\int_{H^{(II)}} d^2k \left[\nabla_k \times \vec{A}^{(II)}(\vec{k}) \right]_z + \int_{H^{(I)}} d^2k \left[\nabla_k \times \vec{A}^{(I)}(\vec{k}) \right]_z \right]. \tag{22}$$

To simplify these calculations, we can use the Stokes' theorem and the connection between the potential vectors (21) to write the total Hall conductivity

$$\sigma_{xy} = \frac{e^2}{h} \frac{1}{2\pi i} \oint_{\partial H} d\vec{k} \left[\vec{A}^{(I)}(k_1, k_2) - \vec{A}^{(II)}(k_1, k_2) \right] = -\frac{e^2}{h} \frac{1}{2\pi} \oint_{\partial H} d\vec{k} \cdot \vec{\nabla}_k \phi(\vec{k}) \quad , \tag{23}$$

where ∂H is the interface between the regions $H^{(I)}$ and $H^{(II)}$ of the Brillouin zone. An important remark on the result of (19) is that the Brillouin zone has the shape of a torus. This means that when the Stokes theorem is applied, the Hall conductivity will be zero if the vector $\vec{A}$ can be uniquely defined in the whole torus.

To end the calculation of the Hall conductivity, we must determine $\phi(\vec{k})$. To do this, lets recall the expression (17) and simplify it with a little of algebra.

$$\begin{aligned} e^{i\phi(\vec{k})} &= \left[\frac{m_\tau + |\epsilon(\vec{k})|}{m_\tau + |\epsilon(\vec{k})|} \right] \left[\frac{|\hbar v_F(\tau k_x + ik_y)|}{\hbar v_F(\tau k_x + ik_y)} \right] \\ &= \left[\frac{\hbar v_F |\vec{k} e^{i\tau\theta}|}{\hbar v_F |\vec{k}| e^{i\tau\theta}} \right] = e^{-i\tau\theta}. \end{aligned} \tag{24}$$

By inserting this result in (23) and considering ∂H as small circle of radius k around the $\vec{K}$ point ($\tau = 1$), we obtain

$$\sigma_{xy} = -\frac{e^2}{\hbar} \frac{1}{2\pi} \int_0^{2\pi} kd\theta \left(-\frac{1}{k} \partial_\theta \theta \right) = \frac{e^2}{\hbar}. \tag{25}$$

Now that we have calculated the Hall conductivity in the Haldane model, lets us finish this section discussing how the topological index, the wave function and the Berry curvature (and consequently, the Hall conductivity) change when the parameters of the Hamiltonian are varied. The phase diagram of the Haldane model, sketched in panel (a)

of figure 5 was first obtained by Haldane, to classify the different topological phases in the model as a function of the parameters of the system. The phase diagram has three regions of interest, each one labeled with a different Chern number ν.

The region that corresponds to the limit $|M| > 3\sqrt{3}t_2 \sin(\varphi)$ has $\nu = 0$, hence does not present quantum Hall effect. The absence of the Hall conductivity can be viewed by evaluating the limit $|M| > |3\sqrt{3}t_2 \sin(\varphi)|$ in the explicit forms of the wave functions $\psi^{(I)}$ and $\psi^{(II)}$. If we set for example $M > 3\sqrt{3}t_2 \sin(\varphi)$ the wave function $\psi^{(I)}$ becomes singular at the Dirac point $\vec{K}$, but the whole Brillouin zone can be described by $\psi^{(II)}$. As a result, the vector potential $\vec{A}$ is uniquely defined in the Brillouin zone, leading to a zero Chern number. Figure (5) (b) illustrates the Berry curvature inside the Brillouin zone for different ratios t_2/M. In the limit $M > 3\sqrt{3}t_2 \sin(\varphi)$ we can see that the Berry curvature in both Dirac points have opposite values. If we consider $M < -3\sqrt{3}t_2 \sin(\varphi)$ we have a similar situation, but in this case the whole Brillouin zone will be described by the function $\psi^{(I)}$. To summarize, we can say that in the limit of $|M| > 3\sqrt{3}t_2 \sin(\varphi)$ the system behaves as a trivial insulator.

In the region where $|M| < |3\sqrt{3}t_2 \sin(\varphi)|$ we have a non-zero Chern number ($\nu \neq 0$), but the value of this constant depends on the phase φ. If the phase φ is positive, the Chern number $\nu = 1$ (this is the case that we have described through this section). If the phase φ is negative, the domain of validity of the eigenfunctions in the Brillouin zone is exchanged, which means that $\psi^{(I)}(\vec{k})$ will be valid in H^{II} and $\psi^{(II)}(\vec{k})$ will be defined in $H^{(I)}$, giving a Chern number $\nu = -1$. Observing Figure (5) (b), we can see that the Berry curvature will be equal in both Dirac points and the sign of the curvature will be given by sign of φ.

In the region where $|M| = |3\sqrt{3}t_2 \sin(\varphi)|$ the gap closes at one of the Dirac points (see figure 4), hence the Chern number becomes ill defined and as a consequence we cannot provide a value for the Hall conductivity. Even without a Chern number to classify the state of the system, it can serve to detect a change in the Berry curvature due to the

variation of the parameters. To make this more clear, lets make the following thought experiment. If we consider Figure (5) (b) and now suppose that the system is in the trivial phase with zero Chern number, and then increase the value of $t_2 = 0$ to $t_2 = \Delta$, where $\Delta > 0$ and $M > 3\sqrt{3}t_2 \sin(\varphi)$ even with the increment of t_2 the value of the energy offset between the sub-lattices M makes the system behaves as a trivial insulator. Conversely, if we decrease M the bands close at $M = 3\sqrt{3}t_2 \sin(\varphi)$, and then the gap is reopened to achieve a topological state with Chern number $\nu = 1$. If the parameters of the system are varied slowly, the Chern number of the system can only change if there is a gap closing/gap opening mechanism. The closure and the reopening of the band gap serves as an intuitive tool to detect the changes on the Chern number ν.
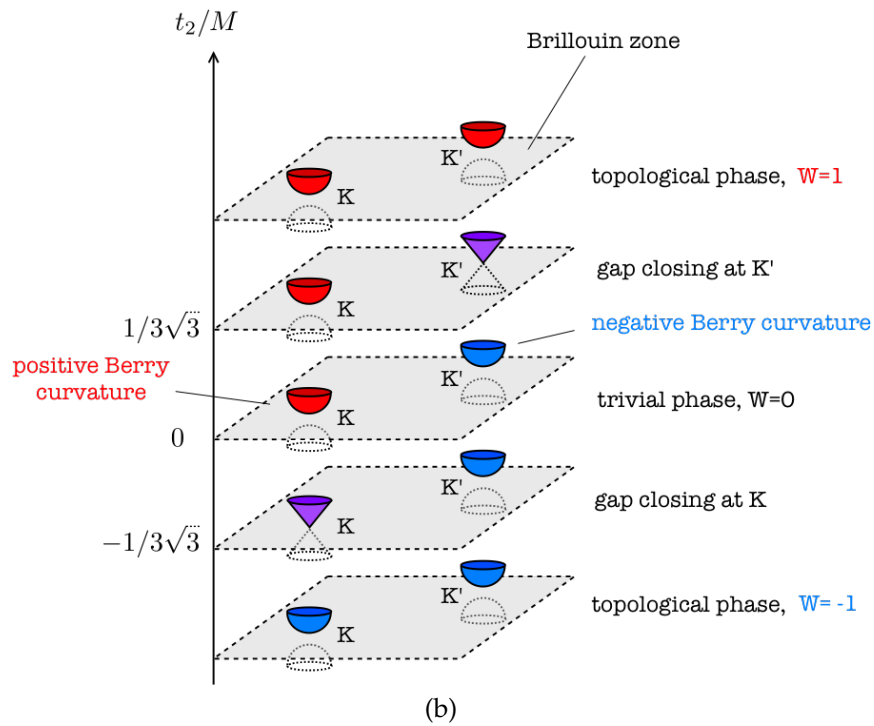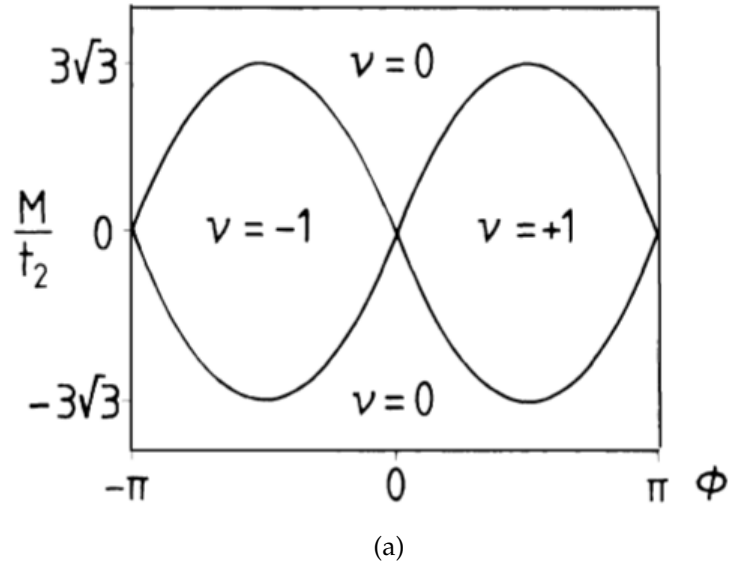
Figure 5: (a) Phase diagram of the Haldane Model. (b) Schematic structure of the berry curvature in the Haldane model.

As final remark on this topic, we must clarify that the only thing that is physical about the singularities present in the wave functions across the whole Brillouin zone is their existence. The localization of the singularities in the Brillouin zone can be altered by performing a gauge transformation, but their sole existence shows that the system

presents a non zero topological index.

We obtained the eigenvalues of the Haldane model and used the low-energy approximation to discuss what are the required conditions for the system to exhibit a quantum Hall state. Now, to study the behavior of the anomalous part of the conductivity in the Haldane model when magnetic fields are applied, we need to include in the tight-binding Hamiltonian of the Haldane model the information of the interaction between the electrons and the applied magnetic field. The next section will be focused on the use of the Peierls substitution to include the information related to the interaction between external magnetic fields and the electrons in the tight-binding Hamiltonian.

2.5 PEIERLS PHASE

In the previous section, we used the structural properties of the honeycomb lattice together with the tight-binding Hamiltonian (4), to find the band structure for the Haldane model and discuss some of its topological properties. In this section we modify the Hamiltonian (4) to include the effect of an external magnetic field. For this purpose, we use the Peierls substitution [33].

The first step in the implementation of the Peierls substitution consists in the multiplication of each hopping term in (4) by a complex phase factor

$$
H = \left[-t \sum_{\langle i,j \rangle} e^{i\phi_{ij}} a_i^{\dagger} b_j + \frac{M}{2} \sum_{i=1}^{D} \left(a_i{}^{\dagger} a_i - b_i{}^{\dagger} b_i \right) \right] + h.c + t_2 \sum_{\langle\langle i,j \rangle\rangle} \left[e^{i(\varphi + \phi_{ij})} a_i^{\dagger} a_j + e^{-i(\varphi - \phi_{ij})} b_i^{\dagger} b_j \right],
$$

$$(26)$$

where the phase ϕ_{ij} holds the information of the interaction between the external magnetic fields and the electrons while they hop from site i to site j, and is defined as:

$$\phi_{ij} \equiv \frac{2\pi}{\Phi_0} \int_{\mathbf{R_i}}^{\mathbf{R_j}} \vec{A} \cdot d\vec{l}. \tag{27}$$

Observing (27), it is clear that the Peierls phase depends mainly on two vectorial quantities: The vector potential $\vec{A}$, which is related to the external magnetic field and the differential $d\vec{l}$ that is related to the crystalline structure of the system. To adapt the general formula (27) to the case of our interest, we have to write the vectors $\vec{A}$ and $d\vec{l}$. First, let us define the vector potential

$$\vec{A} = (-By, 0, 0) \quad , \tag{28}$$

according to Landau's gauge. This vector potential is related to the external magnetic field by $\vec{B} = \vec{\nabla} \times \vec{A}$. To write the differential $d\vec{l}$, we have to define the vector that connects the sites i and j. Using the simplest parametrization, the vector $\vec{l}$ is written like:

$$\vec{l} = \left((X_j - X_i)\tau + X_i \right) \hat{x} + \left((Y_j - Y_i)\tau + Y_i \right) \hat{y} \qquad \tau \in [0,1] \quad , \tag{29}$$

where the pair (X_i, Y_j) represents the coordinates of the site i in the lattice.

To obtain $d\vec{l}$ we just have to differentiate (29) with respect to the parameter τ. By doing this, we obtain:

$$d\vec{l} = (X_j - X_i)\hat{x} + (Y_j - Y_i)\hat{y}. \tag{30}$$

Inserting the results of (28) and (30) in (27), we find that the Peierls phase acquired by an electron when it hops from i to j is

$$\phi_{ij} = \frac{2\pi}{\Phi_0} \int_0^1 \vec{A} \cdot \frac{d\vec{l}}{d\tau} d\tau = -\frac{By2\pi}{\Phi_0} (X_j - X_i). \tag{31}$$

The expression (31), is the general form of the Peierls phase for two different lattice sites. The application of this equation to the case of the hopping between the nearest neighbors and the next nearest neighbors, leads to six different phases. Three of these phases are related to the nearest neighbors and the other three are associated with the next-nearest neighbors.

To calculate the Peierls phase either for the nearest neighbors or the next-nearest neighbors, we have to rewrite some factors in (31). Using the primitive vectors of the lattice (1), the factor y can be written as the projection of $\vec{a_2}$ in the y axis like $y = j\vec{a_2} \cdot \hat{y}$, where the constant j counts the number of sites in the $\vec{a_2}$ direction. For the case of the nearest neighbors, we have to substitute the term $(X_j - X_i)$ by the x projection of the nearest neighbors vectors in (2). Doing this, the Peierls phase for the nearest neighbors reads:

$$\phi_i = -\frac{2\pi B j}{\Phi_0}\left(\frac{3a}{2}\right)\vec{e_i} \cdot \hat{x} \qquad \text{with } i = 1,2,3\ldots \quad . \tag{32}$$

Substituting $\vec{e_i}$ by the explicit form of the vectors (2), the Peierls phases for the nearest neighbors are:

$$\phi_1 = 0 \quad \phi_2 = \frac{\pi B j A}{\Phi_0} \quad \phi_3 = -\frac{\pi B j A}{\Phi_0} \quad , \tag{33}$$

where $A = \frac{3\sqrt{3}a^2}{2}$ is the area of the unitary cell. Grouping the factors in (33) we obtain:

$$\phi_1 = 0 \quad \phi_2 = \frac{j\pi\phi}{\Phi_0} \quad \phi_3 = -\frac{j\pi\phi}{\Phi_0} \quad . \tag{34}$$

To calculate the phases acquired by an electron when it hops to the next-nearest neighbor, we substitute $(X_j - X_i)$ by the x projection of the next-nearest neighbor vectors $(\vec{v_i} \cdot \hat{x})$. Implementing this change, the Peierls phases are:

$$\phi_4 = \frac{-2\pi B j}{\phi_0}\left(\frac{3}{2}\right)a^2\sqrt{3}, \quad \phi_5 = \frac{2\pi B j}{\phi_0}\left(\frac{3}{2}\right)a^2\frac{\sqrt{3}}{2}, \quad \phi_6 = \frac{2\pi B j}{\phi_0}\left(\frac{3}{2}\right)a^2\frac{\sqrt{3}}{2} \quad . \tag{35}$$

To simplify the phases in (35), we use the relation between the field and the flux. Setting the field $B = \frac{2\phi}{3\sqrt{3}a^2}$, the equation (35) reads:

$$\phi_4 = \frac{-2\pi\phi j}{\Phi_0}, \quad \phi_5 = \frac{\pi\phi j}{\Phi_0}, \quad \phi_6 = \frac{\pi\phi j}{\Phi_0} \quad . \tag{36}$$

At this point, we have the expressions of all the Peierls phases that are relevant for our study, but these are written in terms of $\frac{\phi}{\Phi_0}$. To fully determine these phases, we set periodic boundary conditions to obtain a quantization of the magnetic flux in terms of Φ_0.

The periodic boundary conditions imposes:

$$\phi_{ij}(y = 0) = \phi_{ij}(y = L_y) \quad , \tag{37}$$

where L_y is the total length of the system in the y direction. To determine the relation $\frac{\phi}{\phi_0}$, lets pick one of the phases of (34) and insert it in (37). Evaluating the boundary conditions, we get:

$$\frac{\pi\phi N_y}{\phi_0} = 2\pi k \quad \text{with k} = 1, 2, 3 \ldots \tag{38}$$

In (38), we have used $L_y = N_y \vec{a_2} \cdot \hat{y}$, where N_y is the maximum number of sites in the y direction. After some algebra, we obtain the quotient $\frac{\phi}{\Phi_0}$

$$\frac{\phi}{\Phi_0} = \frac{2k}{N_y} \text{ with } k \text{ integer,} \tag{39}$$

Inserting this result in (34), the phases for the nearest neighbors are:

$$\phi_1 = 0 \quad \phi_2 = \frac{2\pi kj}{Ny}, \quad \phi_3 = -\frac{2\pi kj}{Ny} \quad , \tag{40}$$

Repeating the same process in equation (36), the next-nearest neighbors phases read as:

$$\phi_4 = \frac{-4\pi k j}{N_y}, \quad \phi_5 = \frac{2\pi k j}{N_y}, \quad \phi_6 = \frac{2\pi k j}{N_y} \quad . \tag{41}$$

Now that we have calculated the six Peierls phases associated to the hop of electrons, the tight-binding Hamiltonian of the Haldane model contain the orbital information of the interaction between the electrons in the material and an external magnetic field. To calculate the electronic properties of this Hamiltonian in real space, we use the Kernel Polynomial Method. In the next section we present a brief revision of this method and how to implement it to calculate the density of states of systems of non-interacting fermions.

2.6 KERNEL POLYNOMIAL METHOD

The Kernel Polynomial Method is a technique that allows approximate calculations of certain observables with the use of spectral functions. This technique is commonly employed in its real space formulation [23, 21, 28, 27] due to its parallelizability and low computational resource consumption that scales linearly with the size of the system, allowing simulations of large systems. The possibility of considering very large number of sites makes this method very suitable to study systems with a high degree of disorder [34, 35].

In this section, we present a brief introduction to the Chebyshev polynomials and how one may represent spectral functions as a series expansion in terms of them. We discuss how the truncation of such series generates the so called Gibbs oscillations that affect the convergence of the method. We also show how to use kernels to smooth these oscillations and improve the convergence of the Chebyshev series expansions. We close this chapter presenting an iterative process to calculate the density of states of systems

described by a tight binding hamiltonian.

2.6.1 Chebyshev Polynomials

The Chebyshev polynomials constitute a set of orthogonal polynomials that serve as solutions to the differential equations named after the Russian mathematician Panufty Chebyshev. These polynomials have a wide range of applications that goes from numerical approximations to signal processing and spectral analysis [36, 37]. These polynomials can be classified in two groups, the first kind polynomials labeled with the letter $T_n(x)$ and the second kind $U_n(x)$, which can be obtained from the first kind polynomials using elemental differential calculus.

For polynomial expansions, the most commonly used set is the one comprising those of the first kind, because they are bounded and do not diverge at their domain boundaries, like the polynomials of the second kind. Their finiteness near the boundaries allow us to avoid problems with the convergence of the approximated functions [21]. Here we shall deal with polynomials of the first kind only, but by appropriate changes our results may also be extended to polynomials of the second kind.

One of the most remarkable properties of the Chebyshev polynomials is the possibility of writing them in terms of trigonometrical functions [23, 21]. This property allows to define the first kind polynomials as:

$$T_m(x) = \cos(m \arccos(x)) \qquad \text{with} \qquad x \in [-1, 1] \tag{42}$$

The Chebyshev polynomials form an orthonormal basis in the $[-1, 1]$ interval. The orthogonality relation for the polynomials of the first kind is given by

$$\int_{-1}^{1} \frac{T_n(x) T_m(x)}{\sqrt{1-x^2}} dx = \begin{cases} 0 & \text{if } m \neq n \\ \pi & \text{if } m = n = 0 \\ \frac{\pi}{2} & m = n \neq 0 \end{cases} \tag{43}$$

The results of (43) imply that any function $f(x)$ defined in the interval $[-1, 1]$ may be expanded in terms of Chebyshev polinomials:

$$f(x) = \sum_{m}^{\infty} \mu_m T_m(x) \quad, \tag{44}$$

where the μ_m are the coefficients of the expansion. From the orthogonality relations of (43), the coefficients are defined by

$$\mu_m = \frac{2}{1 + \delta_{n,0}} \int_{-1}^{1} \frac{f(x) T_m(x)}{\pi \sqrt{1-x^2}} dx \quad. \tag{45}$$

When the Chebyshev polynomials are compared with the Jacobi or Legendre polynomials, one finds that their distinctive properties make them more efficient for numerical calculations. One of the properties responsible for their efficiency is the recurrence relation

$$T_{m+1}(x) = 2x T_m(x) - T_{m-1}(x) \quad, \tag{46}$$

which allows the construction of any Chebyshev polynomial for $m > 1$. Another property is the minimal ∞-norm when compared with the Jacobi polynomials [38, 36]. However, when we apply them in series representations, some difficulties arise. For example, if the Chebyshev expansion is truncated, it leads to the appearance of the so-called Gibbs oscillations.

2.6.2   Chebyshev Expansion and Gibbs Oscillations

More precisely, when a function is represented by an infinite series expansion in terms of Chebyshev polynomials, the expression (44) is correct. However, when it comes to numerical calculations, it is necessary to truncate the series at some point. The natural question that arises is what order of truncation will provide an acceptable convergence? To answer this question it is useful to establish a link between the Chebyshev and Fourier expansions.

In the traditional Fourier expansion, the highly oscillating terms contribute less to the function approximation. The same applies to the Chebyshev polynomial expansions, where higher order contributions are usually smaller. In figure 6, we show the first four Chebyshev polynomials. We note that the number of zeros of the Chebyshev polynomials increases linearly with their order, while their oscillatory behaviors intensify. One then intuitively expects that higher order Chebyshev polynomials will introduce more oscillatory contributions to the function approximation, though of smaller amplitudes, since the series converge.
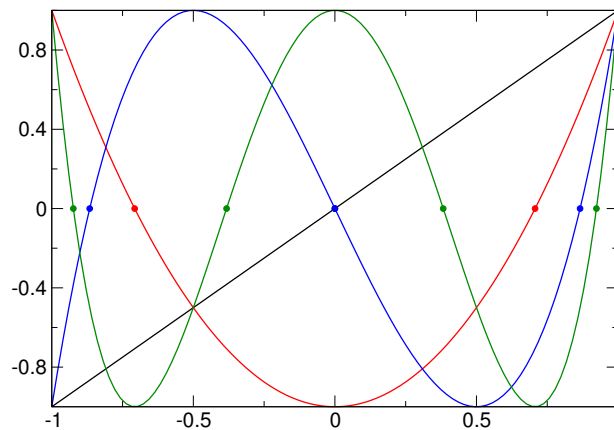

Figure 6: First four order of the Chebyshev polynomials with their roots.

With this idea in mind, we proceed to expand functions in the Chebyshev basis to check if our intuitive reasoning is correct. In panel (a) of figure 7, we show the expansion

of $\cos(x)$ for 50 moments ($M = 50$) and we can see that the approximation has converged to the original function. This fast convergence is a consequence of the smoothness of the function. According with Wolf *et al.* [39], the approximation of a k derivable function converges as $\frac{1}{m^k}$, where m is the number of moments. When we compare this figure with the one in panel (b) we note that the expansion of the step function does not converge properly, even for 200 moments, and presents Gibbs oscillations around its discontinuity.

Unlike the case illustrated in figure 7 (a), the step function is not infinitely differentiable and has a point of discontinuity. This reduces the speed of convergence to $\frac{1}{m}$, which means that we are going to need many more moments to eliminate the oscillations in the expansion and obtain optimal convergence. This short example enable us to verify that the optimal order of truncation will vary according to the properties of the function that we want to expand; if we expand smooth functions, we are going to need less polynomials than the required quantity to expand discontinuous functions.
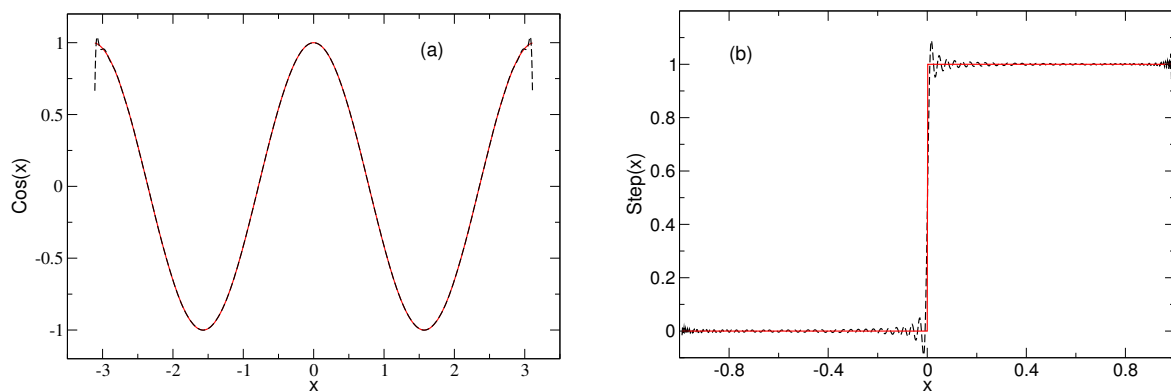
Figure 7: Comparison between the Chebyshev expansion and the analytical function for: (a) $\cos(x)$ with 50 moments and (b) $Step(x)$ with 200 moments.

In solid state physics, the typical functions of interest, like Green functions or Dirac distributions are not infinitively derivable and present discontinuities, which means that if we want to eliminate the Gibbs oscillations in the expansions of these functions by pure force, we are going to need a huge quantity of moments in our expansion, increasing the computational costs. An alternative way to treat this problem is the optimization of the number of moments required in the expansion. Such optimization is

archived by performing a regularization of the function near of the discontinuity points, in order to make the approximation more smooth and eliminate the Gibbs oscillations.

The disadvantage of this regularization process is the inclusion of errors caused by the information loss in the function $f(x)$. An adequate regularization process must guarantee the recover of the information provided by the original function when the order of truncation is increased. The regularization process for the Chebyshev expansion consists in the inclusion of a damping factor that multiplies the coefficients of the expansion and depends of the total number of moments M. Introducing this damping factor, the Chebyshev expansion can be rewritten as:

$$f(x) = \sum_{m=0}^{M} \mu_m T_m(x) \rightarrow f(x) = \frac{1}{\pi\sqrt{1-x^2}} \left(\sum_{m=0}^{M} \mu_m g_m T_m(x) \right) \quad , \tag{47}$$

and the coefficients will be calculated following

$$\mu_m = \int_{-1}^{1} \frac{f(x)T_m(x)}{\pi\sqrt{1-x^2}} dx \longrightarrow \mu_m = \int_{-1}^{1} f(x)T_m(x)dx \quad , \tag{48}$$

to favor the iterative calculation of the moments.

The factor g_m is is called kernel [23, 21] and there are various kernels that can be used for this set of polynomials. Roughly speaking, all kernels that ensure the optimal resolution and the preservation of the norm should fulfill three conditions [21]: The first damping factor should be $g_0 = 1$, the second damping factor when $M \rightarrow \infty$ should converge to $g_1 \approx 1$ and the kernel $K(x, y) = g_0 T_0(x)T_0(y) + 2\sum_{n=1}^{M} g_m T_n(x)T_n(y)$ must be positive in the interval $[-1, 1]$. There are a wide variety of kernels that can be used with the kernel polynomial method. In table 1, we present the most used kernels that fulfill the three conditions.

Table 1: Kernels that can be used in the KPM. M represents the maximum order of truncation, m are the current order. The parameter λ is the adjustment factor of the Lorentz Kernel.

Kernel	Numerical Expression
Jackson	$\frac{1}{M+1}\left[(M-m+1)\cos(\frac{\pi m}{M+1}) + \sin(\frac{\pi m}{M+1})\cot(\frac{\pi}{M+1})\right]$
Lorentz	$\dfrac{\sinh(\lambda(1-\frac{m}{M}))}{\sinh(\lambda)}$
Fejer	$1 - \dfrac{m}{M}$
Dirichlet	1

Dirichlet and Fejer kernels are not optimal, but they are used in the deduction of the Jackson and Lorentz kernels. In this thesis we use the Jackson's kernel and this choice is based on the fact that it has better energy resolution than the Fejer kernel, without adding an extra parameter like the Lorentz kernel. Some of the properties that the Jackson kernel shares with most of the kernels are its positiveness, its dynamic damping which varies as a function of the moments m and M, and the capability of preserving the norm and the integral of the original function.
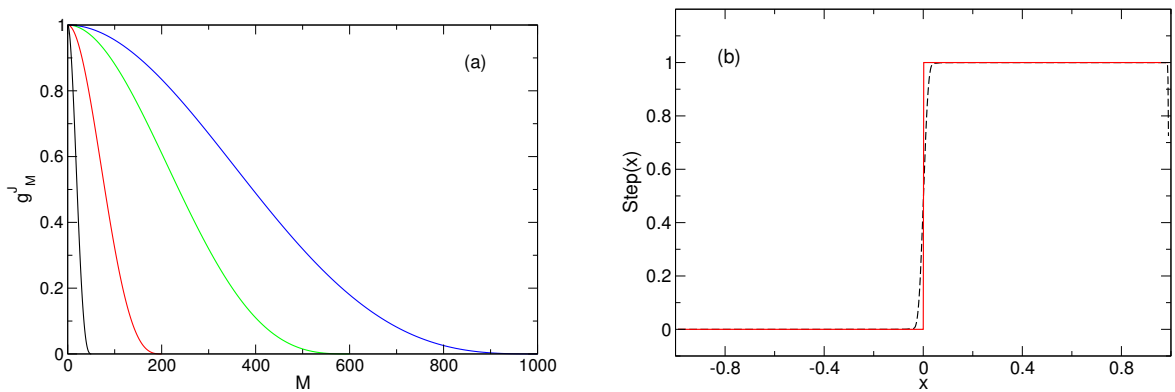

Figure 8: (a) Jackson kernel for: 50 (black), 200 (red), 600 (green) and 1000 moments (blue). (b) Comparison between the step function (solid line) and the approximation with Jackson kernel for 200 moments.

In figure 8 (a) , we show how the damping of the Jackson kernel varies as a function of the expansion moments. From this figure, we can see that the amplitude of the Jackson kernel decays more slowly when the number of moments is increased, this behavior is in agreement with the condition for an optimal regularization. In figure 8 (b) we can observe how the introduction of Jackson kernel improves the convergence of the approximation of the step function and smooths the Gibbs oscillations. After presenting the use of kernels in Chebyshev expansions, we are ready to perform the expansion of spectral functions such as the density of states.

2.6.3 Kernel Polynomial Method: Expansion of the Density of States

In previous subsections, we have made a short revision of the Chebyshev polynomials and how they can be used to expand functions. We discussed the use of kernels to improve the convergence of truncated expansions in terms of Chebyshev polynomials in order to optimize the computational resource consumption. In this subsection, we show the iterative scheme proposed by Silver *et al.* [23, 24] to calculate the density of electronic states. First let us define the density of states $\rho(E)$ of a system of non-interacting fermions:

$$\rho(E) = \frac{1}{D} \sum_{k=0}^{D-1} \delta(E - E_k) \tag{49}$$

To expand the density of states in the Chebyshev basis with KPM, one should perform a rescaling process so that the spectra of the rescaled Hamiltonian is confined to the interval $[-1, 1]$. The rescaling of these elements will be given by:

$$\tilde{H} = \frac{(H - b)}{a} \qquad \tilde{E} = \frac{(E - b)}{a} \quad , \tag{50}$$

where

$$a = \frac{(E_{max} - E_{min})}{(2 - \epsilon)} \qquad b = \frac{(E_{max} + E_{min})}{2} \tag{51}$$

After rescaling the density of states, the next step is to calculate the moments. For this purpose, we use (48), and substitute $f(x)$ by the rescaled density of states to obtain

$$
\begin{aligned}
\mu_n &= \int_{-1}^{1} \rho(\tilde{E}) T_n(\tilde{E}) d\tilde{E} = \frac{1}{D} \sum_{k=0}^{D-1} T_n(\tilde{E}_k) \\
&= \frac{1}{D} \sum_{k=0}^{D-1} \langle k | T_n(\tilde{H}) | k \rangle = Tr\left[T_n(\tilde{H})\right] .
\end{aligned}
\tag{52}
$$

With this we have all the ingredients that we need to perform the description of the electronic states of a system in the tight binding Hamiltonian [28].

2.7 NUMERICAL RESULTS

In this chapter, we presented the Haldane model and its topological properties, and we used the Peierls substitution to include the effects of external magnetic fields in the tight binding Hamiltonian and we showed how to use the Kernel Polynomial Method to calculate the density of states in systems of non-interacting fermions. In this section we present the results of the application of the Kernel Polynomial to study the electronic properties of the Haldane model in presence of an external magnetic field.

2.7.1 Field Symmetry Breaking

In the past sections, we modified the Haldane tight-binding Hamiltonian to consider the effect of an external magnetic field acting on the electrons. With this new Hamiltonian we calculated the density of states (DOS) with the Kernel Polynomial Method (KPM). In figure 9, we show the results of our numerical calculation of the density of states for the

case of graphene ($t_2 = M = 0$). In this figure we can note that the spectrum for particles and holes of the system is the same for both the field configurations. The existence of the landau level $n = 0$ at the band center reveals that this state is shared for both particles and holes (charge conjugation symmetry).
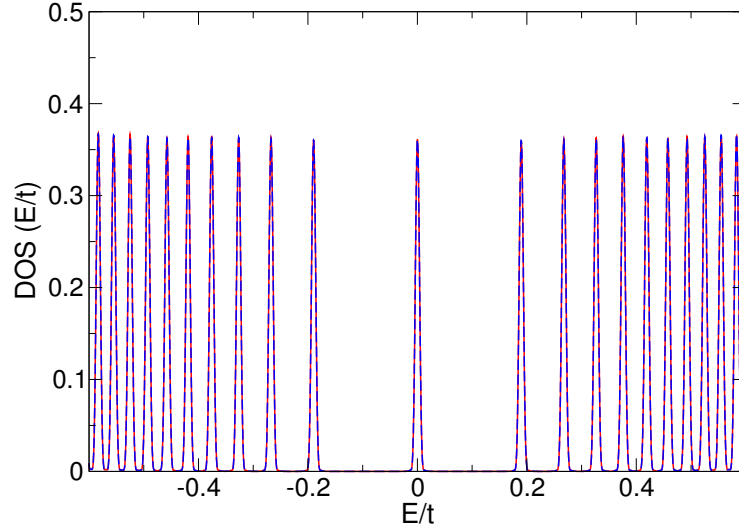

Figure 9: Density of states of the Haldane model for a system of $2 \times 100 \times 600$, $t_2 = 0$ in units of t and for the fields: $B = 50T$ (dashed line) and $B = -50T$ (solid line).

After performing the numerical calculation of the DOS for the case of the graphene, we have proceeded to calculate the DOS for the Haldane model, shown in figure 10. Panel (a) presents the DOS of the system with positive and negative magnetic fluxes. From the panel (a) we see that the numerical calculations reproduce the symmetry breaking in $n = 0$, as expected in accordance with the approximations made by Haldane [12]. However, when we check the landau levels with $|n| \geq 1$ we note that these eigenstates are not symmetric under the change of the sign of the field.

To examine in more detail the lack of symmetry in the spectrum with respect to the field, we can change the energy scale. In panel (b) we show the density of states for the same system, but focusing only in the Landau levels $n = 1$ and $n = 2$. In this panel, we can see that the field symmetry breaking seems to be caused by a constant shift that depends on the sign of the field and was ignored in previous analytical calculations.
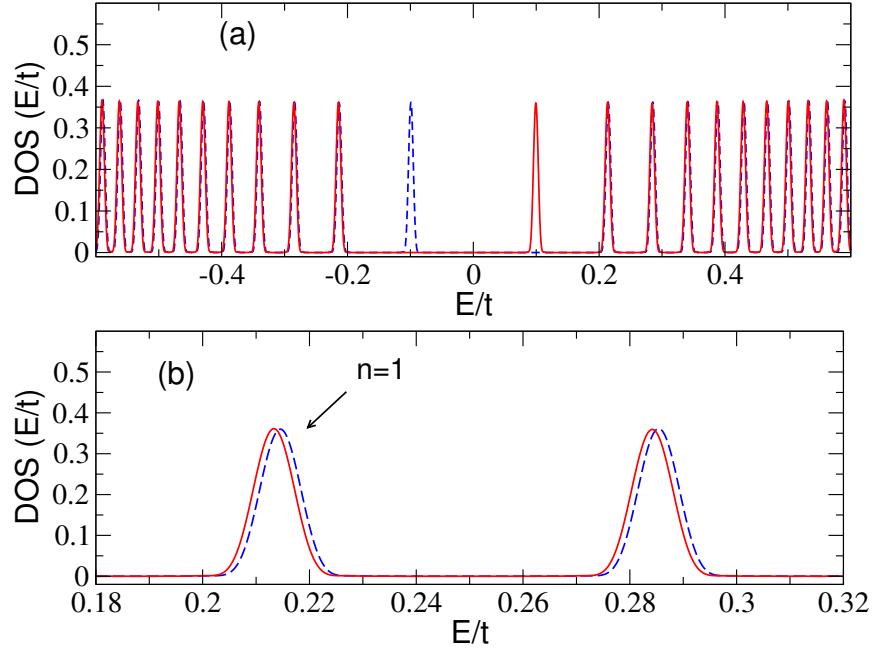

Figure 10: Density of States for Haldane model for a system of $2 \times 100 \times 600$ atoms, $t_2 = \frac{0.2}{6\sqrt{3}}$ in units of t and $|B| \approx 263T$: (a) Comparison between the system with positive flux (dashed line) and negative flux (solid line). (b) Plot of the landau levels $n = 1$ and $n = 2$ for the system with positive flux (dashed line) and negative flux (solid line).

2.7.2   SdH Oscillations on the Hall Conductivity
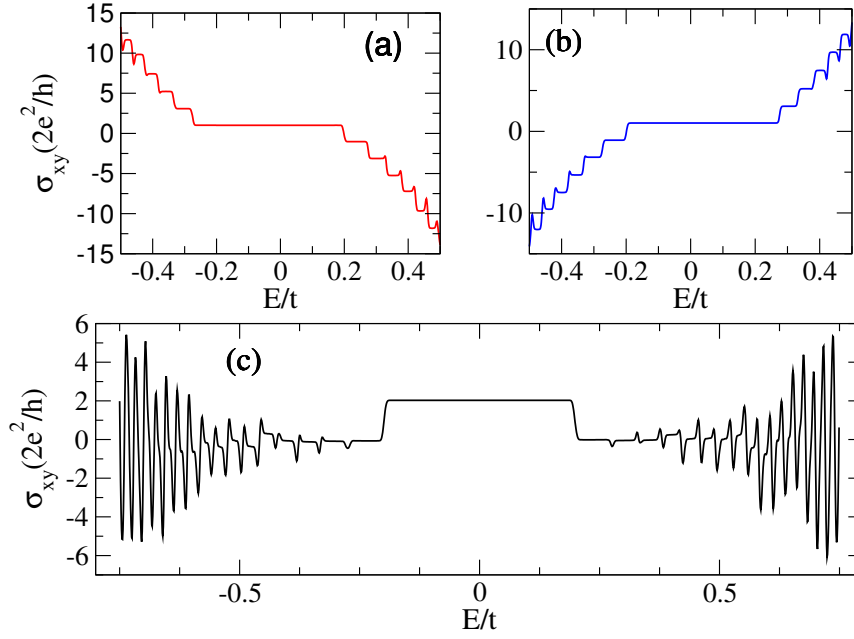
Figure 11: Transverse Conductivity for Haldane Model for a system of $2 \times 100 \times 600$ atoms, $t2 = \frac{0.4}{6\sqrt{3}}$ in units of t and $B = 263T$: Negative Flux (a), Positive Flux (b). Addition of the conductivities with Positive and Negative Fluxes (c).

In the previous subsection, we observed that the spectrum of our system does not preserve its symmetry under a change in the sign of the magnetic field. To study the consequences of this symmetry break in the anomalous part of the Hall conductivity, we use the KPM to calculate the Hall conductivity with the Kubo-Bastin formula [40]

$$\sigma_{\alpha\beta}(\mu, T) = \frac{ie^2\hbar}{\Omega} \int_{-\infty}^{\infty} d\epsilon\, f(\epsilon) \times Tr \left\langle v_\alpha \delta(\epsilon - H) v_\beta \frac{dG^+(\epsilon)}{d\epsilon} - v_\alpha \delta(\epsilon - H) v_\beta \frac{dG^-(\epsilon)}{d\epsilon} \right\rangle \quad , \quad (53)$$

where Ω is the volume of the sample, v_α is the α component of the velocity operator, $G^{(\pm)}(\epsilon, H) = \frac{1}{\epsilon - H \pm i0}$ are the advanced (+) and retarded (−) Green functions, and $f(\epsilon)$ is the Fermi-Dirac distribution for a fixed temperature T and chemical potential μ. The detailed process to expand of the formula (53) with KPM is explained in reference [28].

In figure 11, we show the Hall conductivity for positive (see panel (a)) and negative fluxes (see panel (b)). To obtain the anomalous part of the transverse conductivity, we used the symmetry properties of the contributions to the Hall effect, which states that the anomalous contribution to the Hall conductivity does not change its sign when the applied field is inverted [41]. Knowing this, we have added the Hall conductivities with opposite field sign and same magnitude, to obtain the anomalous part of the Hall conductivity. The anomalous part of the Hall conductivity is plotted in panel (c).

Observing figure 11 (c), we note the persistence of the plateau inside the gap between the bands. This plateau is characteristic of the Haldane model. We can also note some oscillations in the anomalous part of the conductivity. If we compare the position of these oscillations with the position of the energy levels in the density of states of the figure 10, it is clear that the field dependent shift in the spectrum is responsible for the oscillations in the anomalous part of the Hall conductivity. This result, shows the existence of a field dependent shift that was ignored in previous analytical calculations and have important repercussions in the anomalous part of the Hall conductivity. To investigate this shift in the energy spectrum, we will study the analytical continuum model in the next chapter and try to understand the functional form of this shift.

3 | CONTINUUM MODEL: LOW-ENERGY HAMILTONIAN

3.1 INTRODUCTION

In the previous chapter, we used KPM to find a shift in the spectrum of the Haldane model under external magnetic field that depends on the sign of the applied field. This shift was ignored in the original and subsequents theoretical calculations. In this chapter we investigate the origins of this shift in the spectrum and its properties. For that purpose, we decided to study the low-energy continuum approximation, first presented by Haldane [12]. This approximation makes it possible to calculate the energy spectrum analytically to analyse the role of different parameters in the appearance of this energy shift.

It has been shown that considering higher order terms in the expansion of the tight-binding Hamiltonian of graphene near of the Dirac points, provides corrections to the Landau energy spectrum [42, 43]. Motivated by this analysis, in this chapter we consider the next order of the approximation in the expansion of the Haldane tight-binding Hamiltonian near of the Dirac points and use the Landau-Peierls substitution to model the shift in the spectrum. Once the corrected Hamiltonian is obtained, we calculate the Hall conductivity using the formula derived from the movement equations (see A. Ferreira *et al.* [44]) to investigate analytically the dependence of the spectrum on the sign of the external magnetic field and the existence of the oscillations in the anomalous part of the Hall conductivity.

3.2 ZEROTH ORDER APPROXIMATION

Before studying the effects of higher order terms in the expansion of the Haldane tight-binding Hamiltonian near of the Dirac points, let us review the properties of the original version of this low-energy Hamiltonian. To this end, we can use the low-energy Hamiltonian for the Haldane model that was presented in the chapter 2:

$$
H(\vec{k}) = \begin{pmatrix} m_\tau & v_F(\hbar\tau k_x - i\hbar k_y) \\ v_F(\hbar\tau k_x + i\hbar k_y) & -m_\tau \end{pmatrix} ,
\tag{54}
$$

To include the effects of an external magnetic field in (54), we use the Landau-Peierls substitution $\pi_i = p_i - q_e A_i$ to represent the momentum of charged particles in magnetic fields, where we used $q_e = -e < 0$. Substituting $\vec{p} = \hbar\vec{k}$ in (54) by $\vec{\pi}$ we obtained:

$$
H = v_F \left(\tau_z \lambda \pi_x \sigma_x + \pi_y \sigma_y \right) + \Delta_{\tau_z} \sigma_z \quad ,
\tag{55}
$$

The Hamiltonian (55) holds the information of the couplings between the momentum of the particles, the energetic scale (given by the Fermi velocity ($v_F = \frac{3ta}{2\hbar}$)), the isospin in the honeycomb lattice, the choice of the Dirac point ($\tau_z = 1$ for $\vec{K}$ and $\tau_z = -1$ for $\vec{K}'$) and the direction of the perpendicular field ($\lambda = 1$ for $\hat{B} = \hat{z}$ and $\lambda = -1$ for $\hat{B} = -\hat{z}$).

The term Δ_{τ_z} in (55) holds the information of the second nearest neighbor hopping and the inter-lattice potentials. The explicit form of Δ_{τ_z} is the zeroth order expansion of

$$
\mathcal{H}_z(\vec{k}) = M - 2t_2 \sin(\phi) \sum_i \left(\sin(\vec{k} \cdot \vec{v}_i) \right) \qquad \text{with } i = 1,2,3 ,
\tag{56}
$$

in the vicinity of the Dirac points. The vectors $\vec{v}_i$ in (56) describe the relative position between the three inequivalent second-nearest neighbors in the honeycomb lattice, these vectors are:

$$\vec{v}_1 = \left(\sqrt{3}a, 0 \right), \quad \vec{v}_2 = \left(\frac{-\sqrt{3}}{2}a, \ \frac{3}{2}a \right), \quad \vec{v}_3 = \left(-\frac{\sqrt{3}}{2}a, -\frac{3}{2}a \right) \tag{57}$$

Performing a Taylor series expansion of (56) centered in the Dirac point, we note that the major contribution to this expansion is given by the zeroth order term. Considering pure imaginary second neighbor hopping ($\phi = \frac{\pi}{2}$) and zero inter-lattice potential ($M = 0$), the zeroth order of the expansion (56) reads:

$$\Delta_{\tau_z} = \tau_z 3\sqrt{3}t_2. \tag{58}$$

Now, that we defined the term Δ_{τ_z}, we proceed to calculate the eigenstates of the system and their eigenvalues. To do this, we use the Landau quantization to rewrite the Hamiltonian (55) in terms of the ladder operators:

$$\pi_x = \sqrt{\frac{\hbar e |B|}{2c}} \lambda \left(a + a^\dagger \right), \quad \pi_y = \sqrt{\frac{\hbar e |B|}{2c}} \frac{1}{i} \left(-a + a^\dagger \right) \tag{59}$$

and

$$\sigma_x = (\sigma_+ + \sigma_-), \quad \sigma_y = \frac{1}{i}(\sigma_+ - \sigma_-) \tag{60}$$

Inserting the explicit form of these operators and the expansion (58) in (55), we obtain:

$$H = \sqrt{\frac{e\hbar |B|}{2c}} v_F \left[\tau_z \lambda (a\sigma_+ + a\sigma_- + a^\dagger \sigma_+ + a^\dagger \sigma_-) - a^\dagger \sigma_+ - a\sigma_- + a^\dagger \sigma_- + a\sigma_+ \right] + \Delta_{\tau_z}\sigma_z. \tag{61}$$

A valid basis to diagonalize (61) is the basis of the operator $\hat{N} = a^\dagger a + \sigma_+ \sigma_-$, that counts the excitations of the system. The choice of this basis is motivated by the fact that $\hat{N}$ commutes with the effective Hamiltonian [45].

An important feature of (61) is the additional dependence on the direction of the field. This dependence on the field direction is usually ignored, but when it is included, the relative sign between τ_z and λ affects how the linear combinations of the states that diagonalize the Hamiltonian are formed.

The eigenstates of (61) for every $n \geq 1$ are:

$$|\Psi_n\rangle = \begin{cases} \alpha_n |(n-1)A\rangle + \beta_n |(n)B\rangle, & \text{When } \lambda \text{ and } \tau_z \text{ have the same sign} \\ \bar{\alpha}_n |(n)A\rangle + \bar{\beta}_n |(n-1)B\rangle, & \text{When } \lambda \text{ and } \tau_z \text{ have different signs} \end{cases} \tag{62}$$

The eigenstates for $n = 0$ are:

$$|\Psi_0\rangle = \begin{cases} |(0)B\rangle, & \text{When } \lambda \text{ and } \tau_z \text{ have the same sign} \\ |(0)A\rangle, & \text{When } \lambda \text{ and } \tau_z \text{ have different signs} \end{cases} \tag{63}$$

Writing (61) as a matrix in the space spanned by (62), the Hamiltonian for the *Nth* Landau level is:

$$H^{\tau_z \lambda} = \begin{pmatrix} \Delta_{\tau_z} & \tau_z \lambda \sqrt{2|n|} \frac{\hbar v_F}{l_B} \\ \tau_z \lambda \sqrt{2|n|} \frac{\hbar v_F}{l_B} & -\Delta_{\tau_z} \end{pmatrix}, \tag{64}$$

where $l_B = \sqrt{\frac{\hbar c}{e|B|}}$.

Diagonalizing (64), the energy for the nth level reads as:

$$E_n = \eta \sqrt{\Delta_{\tau_z}^2 + \left(\sqrt{2|n|} \frac{\hbar v_F}{l_B} \right)^2} \tag{65}$$

Where η will serve to describe the electrons ($\eta = 1$) and the holes ($\eta = -1$).

3.2.1   Ground State Symmetry Breaking

It was shown by Haldane [12] that the energy of the ground state of this system depends on the relative signal between the magnetic field, the phase of the complex hopping and the choice of the valley. To study this dependence we used the previous model, where we set the valley index $\tau_z = 1$ to make more clear the dependence on the sign of the field. Considering this, the Hamiltonian matrix for the ground state ($n = 0$) is:

- For the positive field ($\lambda = 1$):

$$H = \begin{pmatrix} 0 & 0 \\ 0 & -\Delta_+ \end{pmatrix} \tag{66}$$

- For the negative field ($\lambda = -1$):

$$H = \begin{pmatrix} \Delta_+ & 0 \\ 0 & 0 \end{pmatrix} \tag{67}$$

and the eigenvalues of (66) and (67) are:

$$E_0 = -\lambda \tau_z \left(\Delta_+ \right) \tag{68}$$

3.3   SECOND ORDER CORRECTIONS

Further refinements in the analytical model of the later section can be archived by including the next two terms in the Taylor series expansion of (56). Expanding the $\vec{k}$ dependent term up to second order in the vicinity of one of the Dirac points, we get:

$$\sin((\vec{K} + \vec{q}) \cdot \vec{v}_i) \approx \left(\sin(\vec{K} \cdot \vec{v}_i) \right) + (\vec{q} \cdot \vec{v}_i) \left(\cos(\vec{K} \cdot \vec{v}_i) \right) - \frac{1}{2} (\vec{q} \cdot \vec{v}_i)^2 \left(\sin(\vec{K} \cdot \vec{v}_i) \right). \tag{69}$$

Using the vectors (57), the second order expansion of $\mathcal{H}_z(\vec{k})$ is given by.

$$\Delta_{\tau_z}^{(II)} = M - 2t_2\left(-\tau_z\frac{3\sqrt{3}}{2} + \tau_z\frac{9\sqrt{3}}{8}(\vec{k}a)^2\right) = \Delta_{\tau_z} - \tau_z t_2\frac{9\sqrt{3}}{4}(\vec{k}a)^2 \qquad (70)$$

The expression (70) can be rewritten as

$$\Delta_{\tau_z}^{(II)} = M + \tau_z t_2 3\sqrt{3} - \tau_z\frac{\hbar^2\vec{k}^2}{2m'}, \qquad (71)$$

to get a "Kinetic Energy like" term that help us to simplify the notation. In (71) all the numeric pre-factors were grouped inside of the constant m', which is defined as:

$$m' \equiv \frac{2\hbar^2}{t_2 9\sqrt{3}a^2}. \qquad (72)$$

Using the Landau-Peierls substitution to include the effects of the external magnetic field and neglecting the existence of inter lattice potentials $M = 0$, we rewrite (71) as:

$$\Delta_{\tau_z}^{(II)} = \tau_z t_2 3\sqrt{3} - \tau_z\frac{\left(\pi_x^2 + \pi_y^2\right)}{2m'}. \qquad (73)$$

After inserting the second order corrections of (73) in (55), the Hamiltonian read

$$H = v_f(\lambda\tau_z\pi_x\sigma_x + \pi_y\sigma_y) + \left(\Delta_{\tau_z} - \tau_z\frac{(\pi_x^2 + \pi_y^2)}{2m'}\right)\sigma_z. \qquad (74)$$

To study the effects of the direction of the external magnetic field on the energy spectrum, let us focus on the $\vec{K}$ point ($\tau_z = 1$). The matrix representation of the Hamiltonian for positive fields ($\lambda = 1$) is written like:

$$H^{11} = \begin{pmatrix} \Delta_+ - \frac{\hbar e|B|}{m'c}(a^\dagger a + \frac{1}{2}) & \sqrt{2}\frac{\hbar v_F}{l_B}a \\ \sqrt{2}\frac{\hbar v_F}{l_B}a^\dagger & -\Delta_+ + \frac{\hbar e|B|}{m'c}(a^\dagger a + \frac{1}{2}) \end{pmatrix}, \qquad (75)$$

and for negative fields ($\lambda = -1$) the Hamiltonian is:

$$H^{1-1} = \begin{pmatrix} \Delta_+ - \frac{\hbar e|B|}{m'c}(a^\dagger a + \frac{1}{2}) & -\sqrt{2}\frac{\hbar v_F}{l_B}a^\dagger \\ -\sqrt{2}\frac{\hbar v_F}{l_B}a & -\Delta_+\frac{\hbar e|B|}{m'c}(a^\dagger a + \frac{1}{2}). \end{pmatrix} \qquad (76)$$

From (75) and (76), we note that the inversion of the field direction exchanges the position of the off diagonal terms of the Hamiltonian operator and includes a negative sign on each one of them. This modification in the Hamiltonian changes the Hilbert space that describes the system in the same way that the Hilbert space that describes pristine graphene is altered by the valley inversion.

Evaluating the Hamiltonian matrices (75) and (76) in their respective space of states (62), (63) we get:

- For the positive field ($\lambda = 1$):

$$H = \begin{pmatrix} \Delta_+ - \frac{\hbar e|B|}{m'c}(n - \frac{1}{2}) & \sqrt{2|n|}\frac{\hbar v_F}{l_B} \\ \sqrt{2|n|}\frac{\hbar v_F}{l_B} & -\Delta_+ + \frac{\hbar e|B|}{m'c}(n + \frac{1}{2}) \end{pmatrix} \tag{77}$$

- For the negative field ($\lambda = -1$):

$$H = \begin{pmatrix} \Delta_+ - \frac{\hbar e|B|}{m'c}(n + \frac{1}{2}) & -\sqrt{2|n|}\frac{\hbar v_F}{l_B} \\ -\sqrt{2|n|}\frac{\hbar v_F}{l_B} & -\Delta_+ + \frac{\hbar e|B|}{m'c}(n - \frac{1}{2}) \end{pmatrix}. \tag{78}$$

Diagonalizing (77) and (78), we obtain the the energy for the nth level, with $n \geq 1$:

$$\begin{aligned} E_{n\lambda} &= \lambda \frac{\hbar e|B|}{2m'c} \pm \sqrt{\left(\Delta_+ - \frac{\hbar e|B|}{m'c}|n|\right)^2 + \left(\sqrt{2|n|}\frac{\hbar v_F}{l_B}\right)^2} \\ &= \lambda \frac{\hbar^2}{2m'l_B{}^2} \pm \sqrt{\left(\Delta_+ - \frac{\hbar^2}{m'l_B{}^2}|n|\right)^2 + \left(\sqrt{2|n|}\frac{\hbar v_F}{l_B}\right)^2}. \end{aligned} \tag{79}$$

If we compare the results of (65) and (79), we note that the inclusion of the second order terms in the expansion of $\Delta_{\tau_z}^{(II)}$ produces two mayor corrections. The first is the apparition of a constant factor whose sign is dependent on the field direction, this factor shifts the whole energy spectrum and breaks the symmetry between positive and

negative fields. The second correction is the inclusion of a term which grows linearly with $|n|$ and corrects the contribution of Δ_{τ_z} to the energy of each Landau level.

3.3.1 Ground State Symmetry Breaking

Just like the case of the zeroth order expansion, the model reproduces the ground state symmetry breaking for electrons and holes. If we repeat the same process that was used in the case of the zeroth order expansion of Δ_{τ_z}, we can write the Hamiltonian matrices for the $n = 0$ level:

- For the positive field ($\lambda = 1$):

$$H = \begin{pmatrix} 0 & 0 \\ 0 & -\Delta_+ + \frac{\hbar^2}{m'l_B^2}(\frac{1}{2}) \end{pmatrix} \tag{80}$$

- For the negative field ($\lambda = -1$):

$$H = \begin{pmatrix} \Delta_+ - \frac{\hbar^2}{m'l_B^2}(\frac{1}{2}) & 0 \\ 0 & 0 \end{pmatrix} \tag{81}$$

Diagonalizing (80, 81), we get:

$$E_{0\lambda\tau_z} = -\lambda\tau_z \left(\Delta_+ - \frac{\hbar^2}{2m'l_B^2} \right). \tag{82}$$

Comparing the results of (68) and (82), we note that the second order corrections produce a shift in the energies, even for $n = 0$.

To check if this model represents the special case of the graphene ($t_2 = 0$), we plot (79) for $t_2 = 0$ and $B = 17T$ in figure 12.
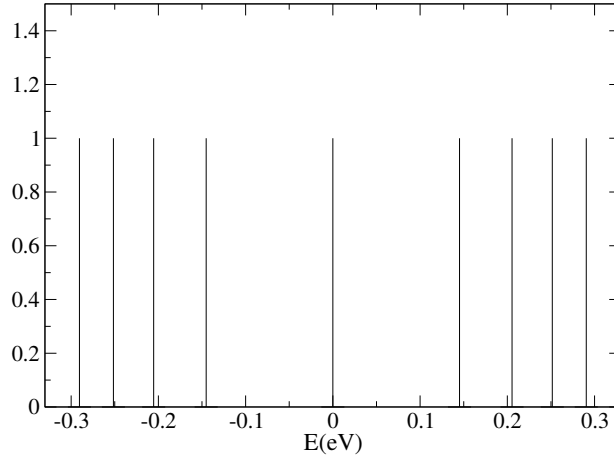
Figure 12: Spectrum of the graphene for: $B = 17T$

In figure 13 we show the Landau levels of the Haldane model for $t_2 = \frac{0.4}{6\sqrt{3}}t$ and $B = 263T$. In the panel (a) we show the comparison between the spectrum of the zeroth order expansion of the Haldane Hamiltonian and the expansion with the second order corrections, for two different field configurations. Panel (b) shows the three first landau levels in an enlarged scale. In the level $n = 1$ we can see the effect of the constant shift that separates the spectrum of positive and negative fields, observing the landau levels $n = 2$ and $n = 3$ we can see the contribution of the term in (79) that corrects the amplitude of Δ_{τ_z} and grows linearly with $|n|$.
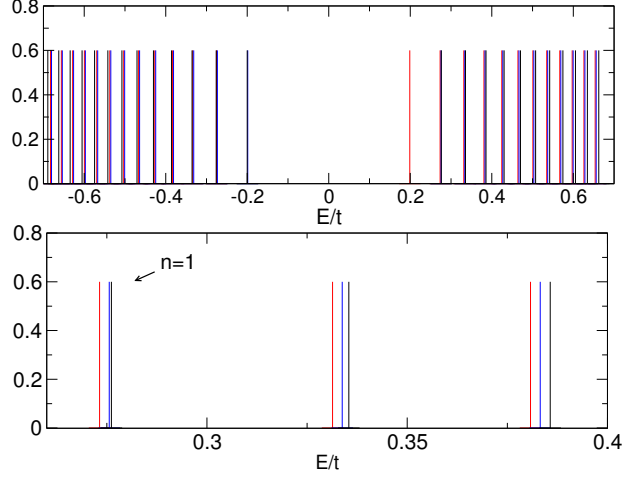
Figure 13: Comparison between the zeroth order expansion of the Haldane model spectrum (black line) and the spectrum with corrections of the order $\mathcal{O}(\vec{k})^2$ for positive (blue line) and negative fields (red line), with $t_2 = \frac{0.4}{6\sqrt{3}}t$ and $|B| = 263T$. (a) Landau levels from $n = -4$ to $n = 4$. (b) Enlarged scale of the Landau levels $n = 1$, $n = 2$ and $n = 3$.

From the later results, it is clear that the second order corrections introduce a constant shift in the spectrum. In the following section, we are going to calculate the Hall conductivity for the two field configurations to observe if the oscillations in the anomalous part of the conductivity are captured by this extended analytical model.

3.4 CALCULATION OF THE CONDUCTIVITY

In the previous section we observed that the inclusion of second order corrections in $\vec{k}$ makes the low-energy model introduce a field dependent constant that shifts the spectrum. In this section, we calculate the Hall conductivity for the two different field configurations, to observe if the oscillations in the anomalous contribution of the Hall conductivity are captured by this extended model.

3.4.1 Eigenstates and Matrix elements of σ_x and σ_y

To calculate the Hall conductivity, we use the Kubo formula in the bubble approximation. For the calculations, we need the normalized eigenstates. From equations (62), (63) and (77) we write the normalized eigenstates as:

$$|\Psi_n\rangle = \frac{1}{\sqrt{1+(\alpha_n)^2}}\left(|(n-1)A\rangle + \alpha_n|(n)B\rangle\right), \tag{83}$$

Where α_n is:

$$\alpha_n = \frac{E_{ss}(n) - \Delta_+ + \frac{\hbar^2|n|}{l_B^2 m'}}{\sqrt{2|n|}\frac{\hbar v_F}{l_B}} \tag{84}$$

and $E_{ss}(n)$:

$$E_{ss}(n) = Sign(n)\sqrt{\left(\Delta_+ - \frac{\hbar^2}{l_B^2 m'}|n|\right)^2 + \frac{2\hbar^2 v_F^2}{l_B^2}|n|}. \tag{85}$$

With the eigenfunctions defined, we need to compute the matrix elements of σ_x and σ_y in this basis. The elements of these matrices are:

$$\langle\sigma_x\rangle_{nm} = \langle n|\sigma_x|m\rangle = \frac{1}{\sqrt{1+(\alpha_n)^2}}\frac{1}{\sqrt{1+(\alpha_m)^2}}[\alpha_n\delta_{|n|,|m|-1} + \alpha_m\delta_{|n|-1,|m|}] \tag{86}$$

and

$$\langle\sigma_y\rangle_{mn} = \langle m|\sigma_y|n\rangle = i\frac{1}{\sqrt{1+(\alpha_n)^2}}\frac{1}{\sqrt{1+(\alpha_m)^2}}[-\alpha_n\delta_{|m|-1,|n|} + \alpha_m\delta_{|m|,|n|-1}]. \tag{87}$$

Transition Rules

Equations (86) and (87) hold an important piece of information: these matrices contain the transitions rules between the states that contributes to the conductivity Hall con-

ductivity. To make emphasis on these rules, let us consider equation (86). The matrix $\langle \sigma_x \rangle_{nm}$ will have non zero elements when $|m| - |n| = \pm 1$. This relation gives rise to two specific cases:

- When m and n have the same sign the transition rule connects two states that belongs to the same band, these transitions are called intra-band.

- When m and n have opposite sign, the transitions connects states that belongs to different bands, because of this property these transitions are called inter-band.
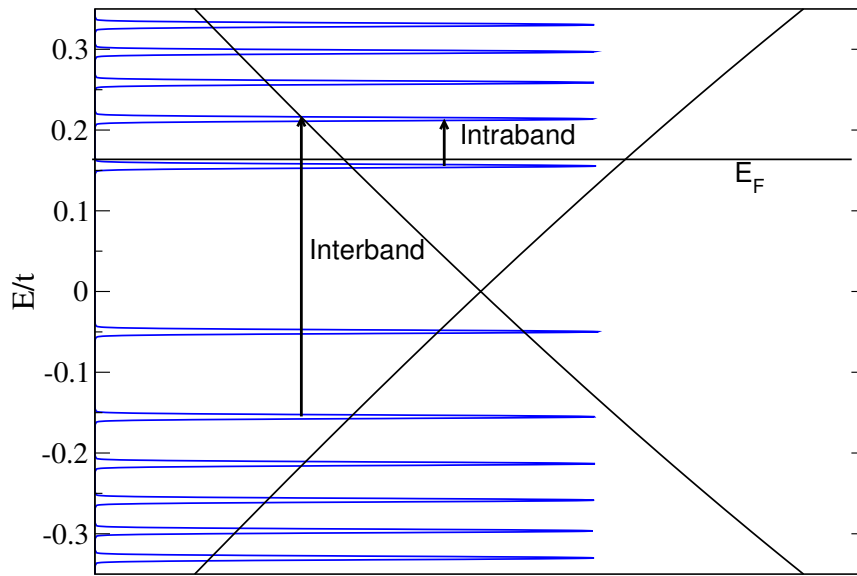

Figure 14: Schematic representation of the transitions that contribute to the conductivity in the Haldane model with $B = 157T$ and $t_2 = \frac{0.1}{2\sqrt{3}} eV$

In Figure 14, we show a schematic representation of the possible transitions that contribute to the conductivity in the Haldane model for a given Fermi energy.

3.4.2 Kubo Formula

To calculate the Hall conductivity, we use the equation of motion method proposed by A. Ferreira *et al.* [44], which after the proper regularization, provides results that are equivalent to the Kubo formula. According to this method, the conductivity is given by

$$
\sigma_{xy} = \frac{e^2}{h} \sum_{n \neq m = -Nc}^{Nc} \frac{\Lambda_{nm}^{xy}}{iE_{nm}} \frac{n_F(E_n) - n_F(E_m)}{E_{nm} + i\Gamma} \tag{88}
$$

where ($t \approx 2.7eV = E_{Nc}$) so that we only consider states that have energy that is lower than the cutoff energies where the low-energy approximation is valid. Λ_{nm}^{xy} is given by:

$$
\Lambda_{nm}^{xy} = \frac{\hbar^2 v_f^2}{l_B^2} \langle \sigma_y \rangle_{mn} \langle \sigma_x \rangle_{nm} = \frac{\hbar^2 v_f^2}{l_B^2} [i \left(\frac{1}{\sqrt{1 + (\alpha_n)^2}} \frac{1}{\sqrt{1 + (\alpha_m)^2}} \right)^2 (\alpha_m{}^2 \delta_{|n|-1,|m|} - \alpha_n{}^2 \delta_{|m|-1,|n|})],
$$

$$
\tag{89}
$$

where E_{nm} represent the energy difference between the n and m levels, Γ represents the broadening of the states and ω is the frequency of an incident photon (we are not considering optical properties of the system, hence $\omega \to 0$).

In figure 15 we show the conductivity for the graphene at fixed field B. One can note that the calculations with the Kubo formula reproduces the structure of the conductivity in the graphene $\sigma_{xy} = 2\frac{e^2}{h} \left(N + \frac{1}{2} \right)$.
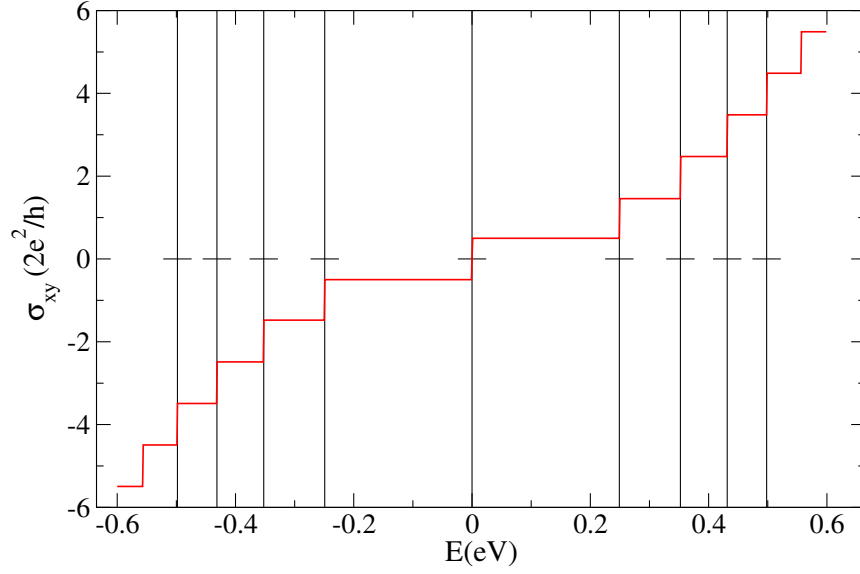
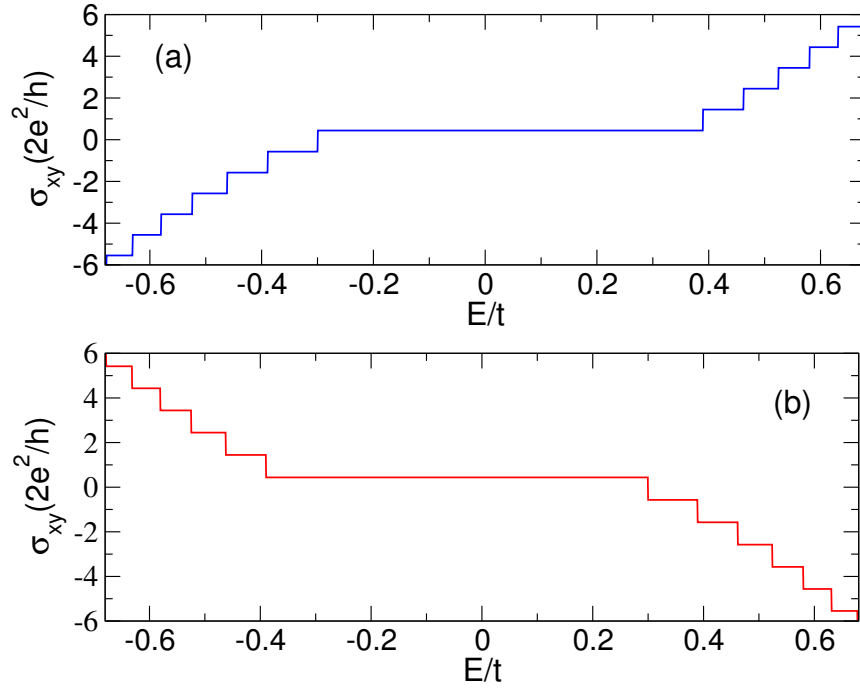Figure 15: Conductivity for the graphene with $B = 50T$ and broadening $\Gamma = 0$.

Figure 16: Calculation of σ_{xy} for the Haldane model with a field $|B| = 50T$, with $t2 = \frac{0.2}{2\sqrt{3}}\ eV$ and broadening $\Gamma = 0.006\ eV$: (a) Positive flux. (b) Negative Flux.

In figure 16, we show the analytical calculations of the transverse Hall conductivity for the Haldane model with the second order corrections. In panels (a) and (b) we plot the conductivity for a system with positive and negative magnetic fields respectively. Comparing 15 and 16, we note that the plateaus of the conductivity in the Haldane model have the half-integer Hall steps, which are present on the case of the graphene. We can also see the plateau with Chern number $n = 0$, which is present in the gap that is characteristic of the Haldane model.

With the analytical calculations of the transverse conductivity in hands, we are able to verify if the theoretical model can capture the existence of the SdH oscillations in the anomalous Hall conductivity. To investigate this, we use the symmetry properties of the Hall conductivity. According with Tsaran *et al.* [41], we can filter the anomalous contributions of the Hall conductivity by adding the net conductivities of the same system, but exposed to opposite magnetic fields.

In figure 17 we show the transverse conductivity for two opposite magnetic fields and their anomalous Hall contribution. In the panels (a) and (b) we show the conductivities for the Haldane model when the second order corrections are included. In the panels (c) and (d) we show the conductivities for the original Haldane model. Comparing the graphics of the panels (a) and (b) with the ones in (c) and (d), we note that the oscillations in the anomalous Hall conductivity are present only in the cases where the second order corrections are considered.
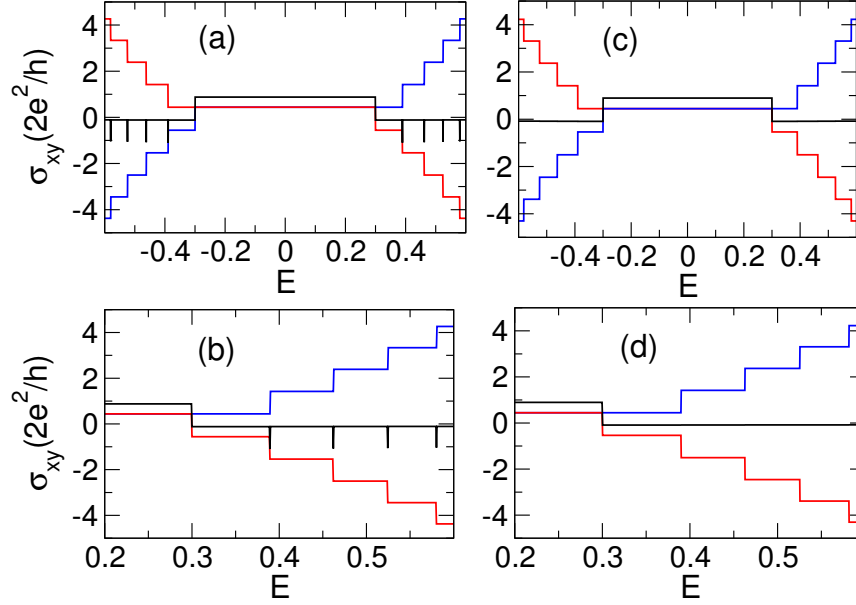
Figure 17: Calculation of the transverse Hall conductivity in the original Haldane model ((c) and (d)) and the Haldane model with second order corrections ((a) and (b)), in a system with $t2 = \frac{0.2}{2\sqrt{3}}$ eV, broadening $\Gamma = 0.012$ eV, for the magnetic fields: $B = 50T$ (blue line) and $B = -50T$ (red line).

In the next final chapter, we compare the theoretical results with the numerical calculations. We compare the energy spectrum of the low-energy model with the second order corrections and the numerical calculations, to verify if the expression that we obtained for the constant term that breaks the field symmetry of the spectrum models the numerical results. We also discuss the limits where the theoretical calculations with the second order correction are valid.

4 COMPARISON: THE NUMERICAL AND ANALYTICAL RESULTS

In the previous chapter, motivated by the results of Y. Supurenko *et al.* [42] and A. Kretinin *et al.* [43], we decided to include terms of order $\mathcal{O}(\vec{k})^2$ to the low-energy expansion of the Haldane model tight-binding Hamiltonian. This extension was aimed to give a theoretical explanation to the difference between the spectrum for positive and negative fields observed in the numerical calculations of chapter 2. We found that the new terms added to the Hamiltonian produce a field-dependent shift in the spectrum, which was ignored in previous works. We calculated the Hall conductivity with this novel Hamiltonian, finding that the oscillations in the anomalous part of the Hall conductivity, found in the numerical calculations of chapter 2, are produced by this constant shift in the spectrum.

In this chapter, we compare the numerical results of the chapter 2 and the analytical results of the chapter 3. We begin by comparing the position of the energy levels in the numerical density of states with the energy of the spectrum of the corrected Hamiltonian with the $\mathcal{O}(\vec{k})^2$ terms. Then, we compare the separation observed between the positive and negative spectrum of the numerical calculations, with the field-dependent shift in (79). By the end of the chapter, we show how the variations of the parameters of the Hamiltonians affect the correspondence between the numerical simulations, the Haldane model and the Haldane model with second-order corrections.

4.1 COMPARISON BETWEEN THEORETICAL AND NU-MERICAL ENERGY OFFSETS.

In this section, we compare the energy spectrum of the original and the extended models with the numerical simulations. In figure 18 we show the comparison between the simulation, the analytical model with the zeroth order terms and the analytical model with second order corrections. In the panels (a) and (b), we show the comparison for the Landau levels $n = 1$ and $n = -1$, respectively. From these plots, we observed that the original model only represents the energy of one of the possible field configurations, meanwhile when the $\mathcal{O}(\vec{k})^2$ terms are included, the extended analytical model gives a good approximation of the energies for both field configurations.
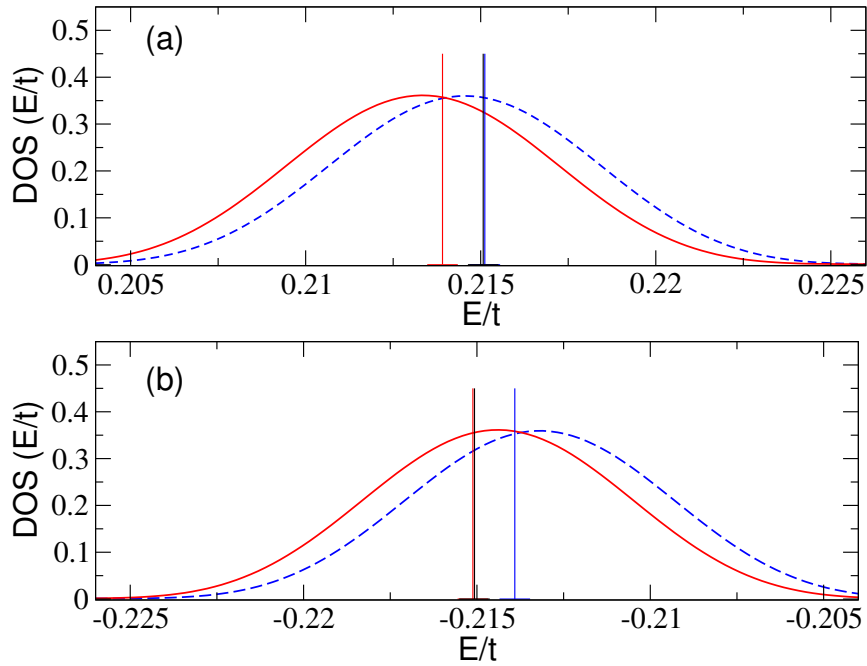

Figure 18: Comparison between the analytical model for the zeroth order expansion (black line), the second order expansions for positive (blue line) and negative (red line) flux, and the numerical calculation for a system of $2 \times 100 \times 600$ sites, $t_2 = \frac{0.2}{6\sqrt{3}}$ and $B = 263T$. (a) comparison for the Landau level with $n = 1$. (b) Comparison for the Landau Level with $n = -1$.

Now that we checked that the eigenvalues of the extended model improves the description of the energy spectrum, we need to check if the field dependent shift that appears in (79) models the field symmetry break in the spectrum. To verify this, we measured the shift between the numerical density of states for different values of t_2 and compared it with the constant term in (79). Figure 19 shows the comparison between the analytical shift and the numerical shift measured as a function of the gap size in the spectrum. From this figure, it is clear that the second-order corrections captures the energy offset that breaks the field symmetry in the spectrum in the limit of high magnetic fields.
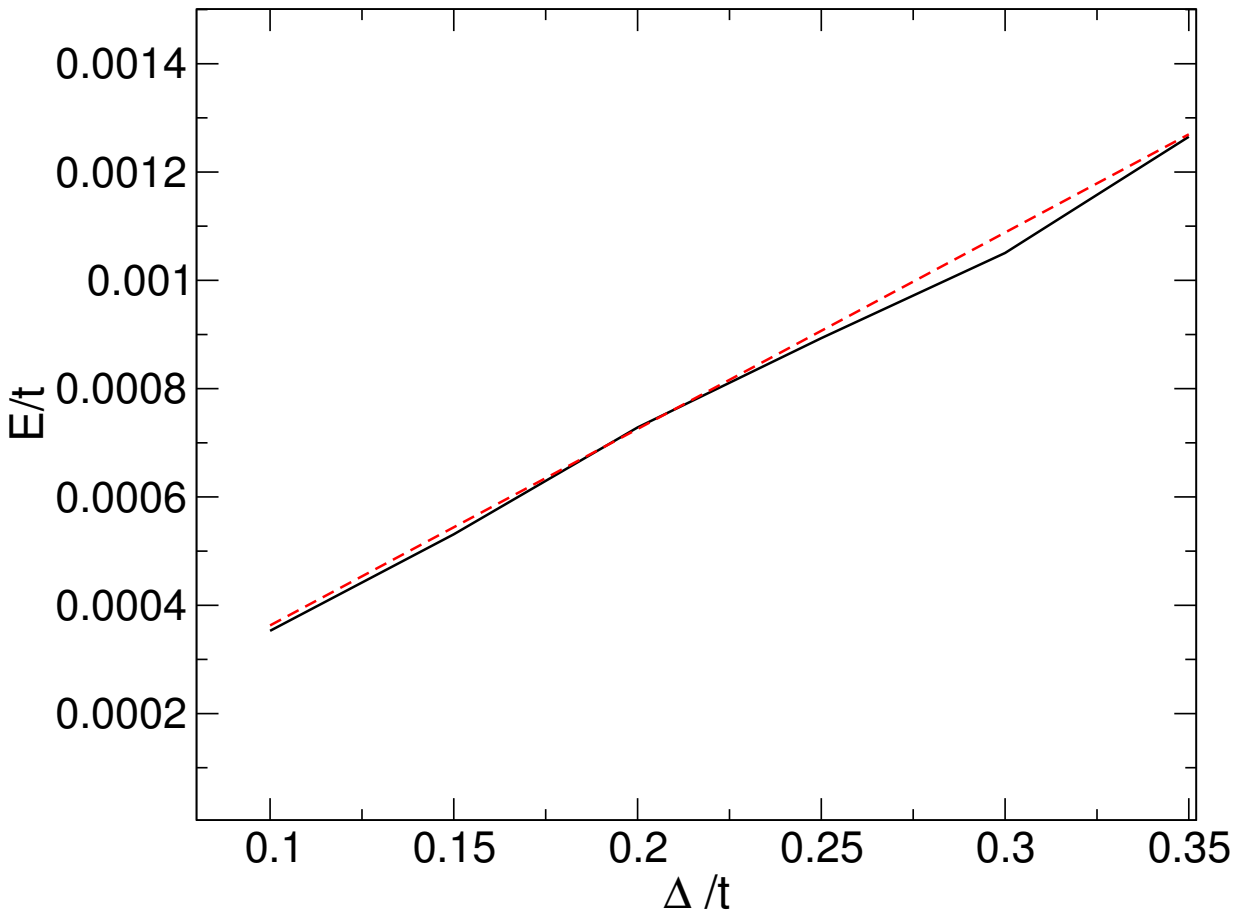

Figure 19: Comparison between the numerical shift (black solid line) and the analytical shift (red dashed line) for a system of $2 \times 1000 \times 1000$ atoms and a field of $B = 157T$.

These results confirms that considering second-order corrections in the low-energy approximation improves the description of the spectrum, making it possible to model

the field-dependent energy offset that breaks the field symmetry in the spectrum. However, this is not the only change in the spectrum caused by the second order corrections. These corrections also include a factor that alters the "Haldane mass" ($\Delta_{\tau_z} = 3\sqrt{3}t_2$) in (79) that instead of being constant, increases linearly with the landau-level count $|n|$.

To investigate the effect of this correction, we took the Landau levels with $|n| = 2$ and compared the original model, the model with the second order corrections and the numerical results for this specific level. In Figure 20, we show the comparison between the original model, the simulation and our extension to the original model for the Landau levels $n = 2$ (panel (a)) and $n = -2$ (panel (b)). Comparing the results of those figures with the ones in figure 18, we can see that for increasing values of $|n|$, the novel terms correct the position of the eigenvalues with respect to the numerical results.

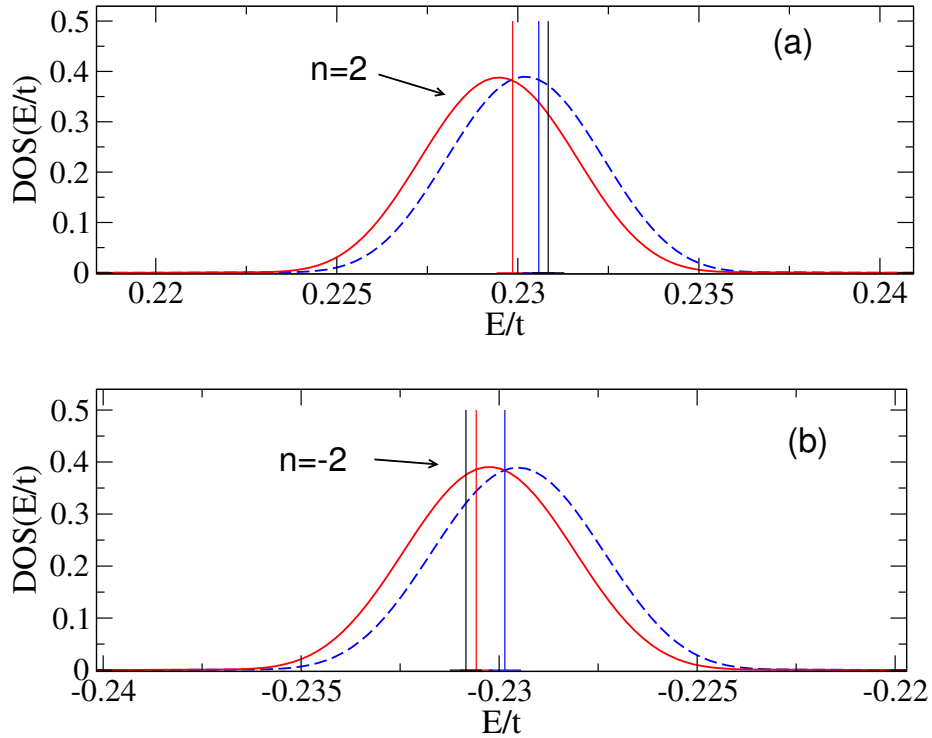Figure 20: Comparison between the analytical model for the zeroth order expansion (black line), the second order expansions for positive (blue line) and negative (red line) flux, and the numerical calculation for a system of $2 \times 100 \times 600$ sites, $t_2 = \frac{0.2}{6\sqrt{3}}$ and $B = 263T$. (a) comparison for the Landau level with $n = 2$. (b) Comparison for the Landau Level with $n = -2$.

From figures 18, 19 and 20, it is clear that even with the improvement of the addition of second-order corrections, when $|n|$ increases, the analytical method reproduces poorly the results obtained with the numerical calculations. In the next section, we discuss how the correspondence between the numerical and the analytical methods is affected by the changes of the parameters of the Hamiltonian.

4.2 RANGE OF VALIDITY OF THE ANALYTICAL APPROXIMATION

In the previous section, we compared the results of the spectrum of the original and extended low-energy expansions with our numerical calculations. We found that the second-order corrections introduce a field dependent constant that models the shift between the spectrum of opposite field configurations. We also noted that the second-order corrections in the low-energy Haldane model improve the description of the energy spectrum, but they do not reproduce exactly the results of the numerical simulations, mainly for higher order of $|n|$. In this section, we study how changes in the parameters $|B|$ and t_2 affect the correspondence between the analytical and the numerical results. To study the influence of these two parameters, we plotted in figures 21 and 23, a comparison of the spectrum for different values of t_2 and B respectively.

In figure 21 we show how the convergence of the model decreases as t_2 increases. The poor representation of the eigenvalues in the limit of high values of t_2 have a strong relation with the band structure of the Haldane model in the absence of magnetic field. In figure 22 we show the comparison between the bands of the Haldane model for two values of t_2 and $t_2 = 0$ (graphene). In this plot, beside the obvious enlargement of the band gap with the increase of t_2, we can appreciate other important feature. In the limit of high values of t_2, the band structure near of the Dirac points does not present the

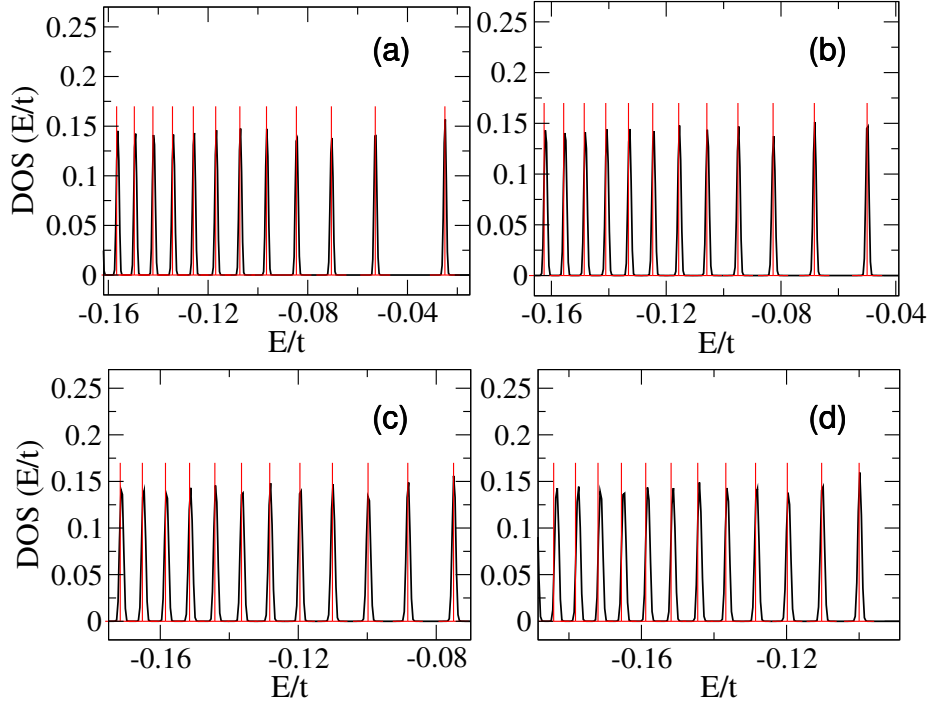conical shape that is found in the graphene, but a more parabolic shape.

Figure 21: Comparison between the theoretical model and the numeric calculations of a system with $2 \times 100 \times 10000$ sites, $B = 15.78T$ and different values of t_2: $t_2 = \frac{0.05}{6\sqrt{3}}$ (a), $t_2 = \frac{0.1}{6\sqrt{3}}$ (b), $t_2 = \frac{1.5}{6\sqrt{3}}$ (c) and $t_2 = \frac{0.2}{6\sqrt{3}}$ (d).

The change in the shape of the band structure gives rise to a zero point energy when the system is exposed to an external magnetic field, in contrast to what is observed in a Dirac-like Hamiltonian. This energy is captured by the low energy model when the second order corrections are included. Beside the appearance of the zero point energy, the increment of t_2 also reduces the number of states that can be exactly described. The low-energy model treats the contribution of the next nearest neighbors terms as a perturbation of pure graphene, so when high values of t_2 are considered the eigenstates required to describe the system must be more complicated linear combinations of states, than the ones used in our approximation.
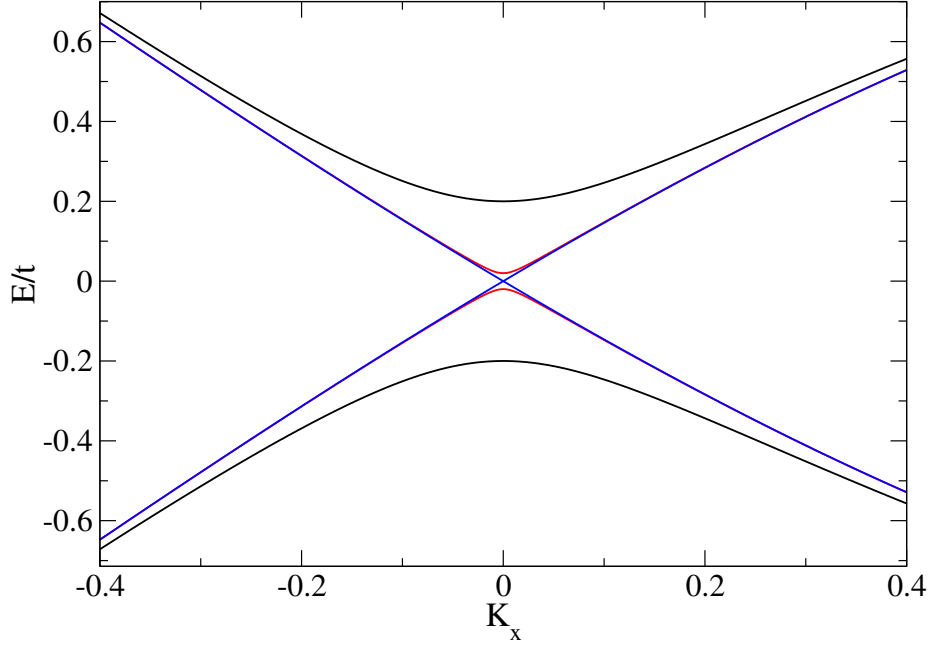
Figure 22: Band structure of the Haldane model for: $t_2 = \frac{0.4}{6\sqrt{3}}$ (Black), $t_2 = \frac{0.04}{6\sqrt{3}}$ (Red) and $t_2 = 0(Blue)$

In figure 23, we show how the correspondence between the theoretical model and the numerical calculations varies when the magnetic field applied on the system is modified. From these results we can observe that the decrement of the magnetic field improves the convergence between the analytical and numerical calculations. The effect of the magnetic field variations in the convergence can be studied in the limit of low values of t_2. Roughly speaking, the difference between two landau levels in this limit will be of the order of $\frac{\hbar}{l_B}\sqrt{2}$. This means that the higher the fields the greater the separation between levels. The increment of the separation between levels will set some levels in the region where the band structure cannot be approximated as a cone, and consequently this reduce the quantity of levels that the theoretical model represents correctly.
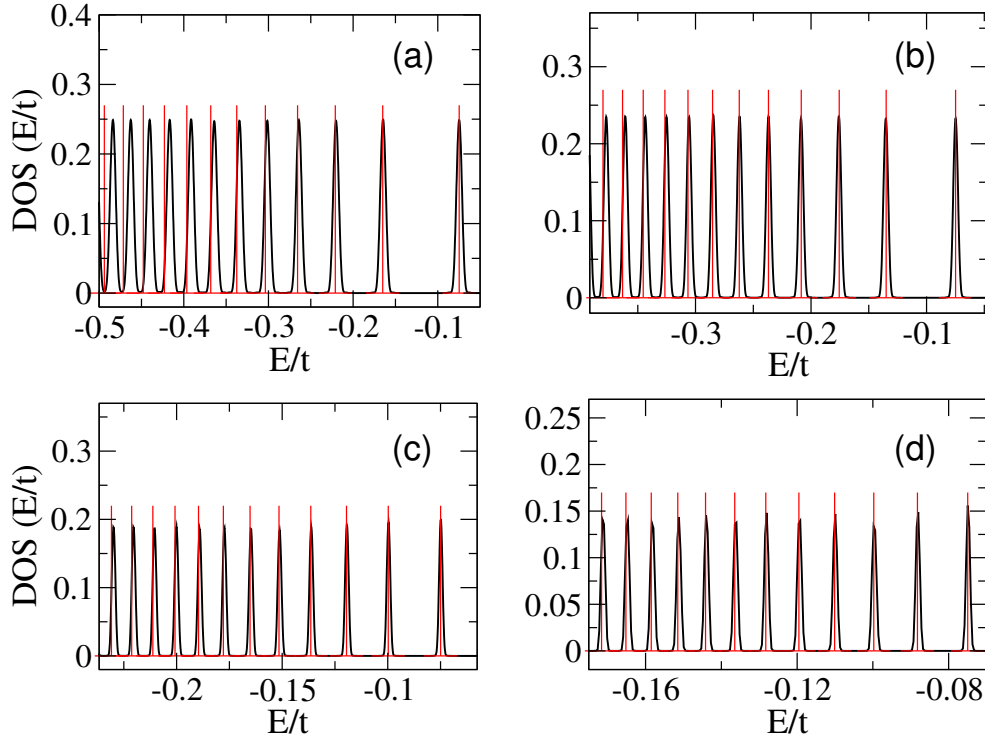
Figure 23: Comparison between the theoretical model and the numerical calculations with $t_2 = \frac{0.15}{6\sqrt{3}}$ in units of t, and different number of sites, for: $2 \times 100 \times 1000$ ($B = 157.78T$) (a), $2 \times 100 \times 1700$ ($B = 92.87T$) (b), $2 \times 100 \times 5000$ ($B = 31.57T$) (c) and $2 \times 100 \times 10000$ ($B = 15.78T$) (d).

In this chapter we have demonstrated that the introduction of the second-order corrections in the low-energy Hamiltonian of the Haldane model reproduces the shift between the spectrum of opposite field configurations. However, we showed that even with the improvements in the low-energy model, the correspondence is affected by the choice of the parameters. We have shown that both the intensity of the field and the value of the next nearest neighbor hopping affects the correspondence between the analytical and numerical spectrum. We observed that increments in the parameter t_2 modify the shape of the band structure and make more notable the zero point energy when the magnetic field is applied to the system.

Also we checked that when high magnetic fields are considered, the correspondence of the analytical model is also affected. To summarize, we can say that the low-energy model reproduces the field dependent shift in the spectrum and is in agreement with the numerical spectrum in the limit of weak magnetic fields and small values of t_2, as should be expected in the case of a perturbative approach.

5 | CONCLUSIONS

In this work we have revisited the quantum Hall effect for the Haldane model, motivated by the behavior of the anomalous part of the Hall conductivity in the high magnetic field limit. In chapter 2, we showed the results of numerical calculations of the density of states and Hall conductivity of the Haldane model under perpendicular magnetic fields using the kernel polynomial method (KPM) for opposite field configurations. From previous calculations, we expected one of the energy levels to be dependent of the sign of the magnetic field but based on low-energy approximations, all the other levels was supposed to remain symmetric under changes of the external field signs. However, we noted a shift between the spectrum of opposite fields together with oscillations in the anomalous part of the Hall conductivity. Both of these results were not predicted by the low-energy expansion implemented by Haldane.

Aiming to explain analytically these results, in chapter 3, we investigated the low-energy expansion of the tight-binding Hamiltonian of the Haldane model. Using the Landau quantization along with the Landau-Peierls substitution, we found the eigenstates and the eigenvalues of the system. Then, motivated by the results of Supurenko *et al.* [42] and Kretinin *et al.* [43] we incorporated the terms of order $\mathcal{O}(\vec{k}^2)$ in the Taylor expansion near of the Dirac point, to the terms related with the next nearest neighbor hopping in the low-energy Hamiltonian.

We calculated the eigenstates and the eigenvalues of this new Hamiltonian and obtained an expression for the energy spectrum which contains a field dependent shift in the spectrum, and a term that adjusts the position of the energy levels and grows

linearly with $|n|$. With these results, we calculated the Hall conductivity and found that the field dependent shift in the spectrum produces oscillations that are similar to the ones observed in the numerical calculations.

After proving that the field dependent shift is responsible for the oscillations in the anomalous part of the conductivity, we proceeded to compare the results of the analytical models (the original and the one with the $\mathcal{O}(\vec{k}^2)$ terms) and the numerical calculations obtained with KPM, to study the improvements in the description of the energy spectrum. By comparing these results, we found that the field-dependent constant in the spectrum of the corrected Hamiltonian reproduces exactly the shift observed in the numerical calculations. Also, it was observed that the effect of the corrections of the terms that adjusts the position of the energy levels becomes more significant when $|n| \ll 1$.

The main result of this thesis is the correction of the energy spectrum of the Haldane model in the limit of high magnetic fields. Unlike the approximative methods that are commonly used in analytical approaches, the numerical calculations performed with KPM allowed us to detect and correct the low-energy Hamiltonian to take into account the differences between the energy spectrum for opposite fields that affect the Hall conductivity and were previously ignored.

Recently the Haldane model has been realized in optical lattices using ultra cold fermionic atoms in a periodically modulated honeycomb lattice [18]. Knowing this we believe that these corrections an be observed in optical lattices where high pseudo magnetic fields can be archived (due the limitation of the lattice size) and the next nearest neighbor hopping intensity (t_2) can assume arbitrary values.

BIBLIOGRAPHY

[1] E. H. Hall, "On a new action of the magnet on electric currents," *American Journal of Mathematics*, vol. 2, no. 3, pp. 287–292, 1879.

[2] K. v. Klitzing, G. Dorda, and M. Pepper, "New method for high-accuracy determination of the fine-structure constant based on quantized hall resistance," *Phys. Rev. Lett.*, vol. 45, pp. 494–497, Aug 1980.

[3] C.-X. Liu, S.-C. Zhang, and X.-L. Qi, "The quantum anomalous Hall effect," *ArXiv e-prints*, Aug. 2015.

[4] M. A. Paalanen, D. C. Tsui, and A. C. Gossard, "Quantized hall effect at low temperatures," *Phys. Rev. B*, vol. 25, pp. 5566–5569, Apr 1982.

[5] D. C. Tsui, H. L. Stormer, and A. C. Gossard, "Two-dimensional magnetotransport in the extreme quantum limit," *Phys. Rev. Lett.*, vol. 48, pp. 1559–1562, May 1982.

[6] R. B. Laughlin, "Quantized hall conductivity in two dimensions," *Phys. Rev. B*, vol. 23, pp. 5632–5633, May 1981.

[7] B. I. Halperin, "Quantized hall conductance, current-carrying edge states, and the existence of extended states in a two-dimensional disordered potential," *Phys. Rev. B*, vol. 25, pp. 2185–2190, Feb 1982.

[8] D. J. Thouless, M. Kohmoto, M. P. Nightingale, and M. den Nijs, "Quantized hall conductance in a two-dimensional periodic potential," *Phys. Rev. Lett.*, vol. 49, pp. 405–408, Aug 1982.

[9] M. V. Berry, "Quantal phase factors accompanying adiabatic changes," *Proceedings of the Royal Society of London A: Mathematical, Physical and Engineering Sciences*, vol. 392, no. 1802, pp. 45–57, 1984.

[10] B. Simon, "Holonomy, the quantum adiabatic theorem, and berry's phase," *Phys. Rev. Lett.*, vol. 51, pp. 2167–2170, Dec 1983.

[11] Q. Niu, D. J. Thouless, and Y.-S. Wu, "Quantized hall conductance as a topological invariant," *Phys. Rev. B*, vol. 31, pp. 3372–3377, Mar 1985.

[12] F. D. M. Haldane, "Model for a quantum hall effect without landau levels: Condensed-matter realization of the "parity anomaly"," *Phys. Rev. Lett.*, vol. 61, pp. 2015–2018, Oct 1988.

[13] G. W. Semenoff, "Condensed-matter simulation of a three-dimensional anomaly," *Phys. Rev. Lett.*, vol. 53, pp. 2449–2452, Dec 1984.

[14] M. Z. Hasan and C. L. Kane, "*Colloquium* : Topological insulators," *Rev. Mod. Phys.*, vol. 82, pp. 3045–3067, Nov 2010.

[15] C.-Z. Chang, J. Zhang, X. Feng, J. Shen, Z. Zhang, M. Guo, K. Li, Y. Ou, P. Wei, L.-L. Wang, Z.-Q. Ji, Y. Feng, S. Ji, X. Chen, J. Jia, X. Dai, Z. Fang, S.-C. Zhang, K. He, Y. Wang, L. Lu, X.-C. Ma, and Q.-K. Xue, "Experimental observation of the quantum anomalous hall effect in a magnetic topological insulator," *Science*, vol. 340, no. 6129, pp. 167–170, 2013.

[16] J. G. Checkelsky, R. Yoshimi, A. Tsukazaki, K. S. Takahashi, Y. Kozuka, J. Falson, M. Kawasaki, and Y. Tokura, "Trajectory of the anomalous hall effect towards the quantized state in a ferromagnetic topological insulator," *Nat Phys*, Oct 2014.

[17] A. Kandala, A. Richardella, S. Kempinger, C.-X. Liu, and N. Samarth, "Giant anisotropic magnetoresistance in a quantum anomalous hall insulator," *Nature Communications*, vol. 6, pp. 7434 EP –, Jul 2015. Article.

[18] G. Jotzu, M. Messer, R. Desbuquois, M. Lebrat, T. Uehlinger, D. Greif, and T. Esslinger, "Experimental realization of the topological haldane model with ultracold fermions," *Nature*, vol. 515, pp. 237–240, Nov 2014. Letter.

[19] C. L. Kane and E. J. Mele, "Z_2 topological order and the quantum spin hall effect," *Phys. Rev. Lett.*, vol. 95, p. 146802, Sep 2005.

[20] D. F. Styer, "What good is the thermodynamic limit?," *American Journal of Physics*, vol. 72, no. 1, pp. 25–29, 2004.

[21] A. Weiße, G. Wellein, A. Alvermann, and H. Fehske, "The kernel polynomial method," *Rev. Mod. Phys.*, vol. 78, pp. 275–306, Mar 2006.

[22] S. Sota and M. Itoh, "Fast and accurate scheme for green functions and eigenvectors: Regulated polynomial expansion without gibbs oscillation," *Journal of the Physical Society of Japan*, vol. 76, no. 5, pp. 054004–054004, 2007.

[23] R. Silver, H. Roeder, A. Voter, and J. Kress, "Kernel polynomial approximations for densities of states and spectral functions," *Journal of Computational Physics*, vol. 124, no. 1, pp. 115 – 130, 1996.

[24] R. N. Silver and H. Röder, "Calculation of densities of states and spectral functions by chebyshev recursion and maximum entropy," *Phys. Rev. E*, vol. 56, pp. 4822–4829, Oct 1997.

[25] Y.-X. Wang, F.-X. Li, and Y.-M. Wu, "Quantum hall effect of haldane model under magnetic field," *EPL (Europhysics Letters)*, vol. 105, no. 1, p. 17002, 2014.

[26] T. Fukui, Y. Hatsugai, and H. Suzuki, "Chern numbers in discretized brillouin zone: Efficient method of computing (spin) hall conductances," *Journal of the Physical Society of Japan*, vol. 74, no. 6, pp. 1674–1677, 2005.

[27] J. H. García, B. Uchoa, L. Covaci, and T. G. Rappoport, "Adatoms and anderson localization in graphene," *Phys. Rev. B*, vol. 90, p. 085425, Aug 2014.

[28] J. H. García, L. Covaci, and T. G. Rappoport, "Real-space calculation of the conductivity tensor for disordered topological matter," *Phys. Rev. Lett.*, vol. 114, p. 116602, Mar 2015.

[29] C. Bena and G. Montambaux, "Remarks on the tight-binding model of graphene," *New Journal of Physics*, vol. 11, no. 9, p. 095003, 2009.

[30] A. H. Castro Neto, F. Guinea, N. M. R. Peres, K. S. Novoselov, and A. K. Geim, "The electronic properties of graphene," *Rev. Mod. Phys.*, vol. 81, pp. 109–162, Jan 2009.

[31] L. Li and S. Chen, "Characterization of topological phase transitions via topological properties of transition points," *Phys. Rev. B*, vol. 92, p. 085118, Aug 2015.

[32] M. Kohmoto, "Topological invariant and the quantization of the hall conductance," *Annals of Physics*, vol. 160, no. 2, pp. 343 − 354, 1985.

[33] R. PEIERLS, *On the Theory of the Diamagnetism of Conduction Electrons*, pp. 97–120.

[34] S. Roche, "Quantum transport by means of O(n) real-space methods," *Phys. Rev. B*, vol. 59, pp. 2284–2291, Jan 1999.

[35] C. H. Wörner and E. Muñoz, "Finite-size corrections to the density of states," *European Journal of Physics*, vol. 33, no. 5, p. 1465, 2012.

[36] A. Gil, J. Segura, and N. Temme, *Numerical Methods for Special Functions*. Society for Industrial and Applied Mathematics, 2007.

[37] J. Boyd and R. Petschek, "The relationships between chebyshev, legendre and jacobi polynomials: The generic superiority of chebyshev polynomials and three important exceptions," *Journal of Scientific Computing*, vol. 59, pp. 1–27, 4 2014.

[38] S. Butenko and P. M. Pardalos, *Numerical methods and optimization: an introduction*. CRC Press, 2014.

[39] F. A. Wolf, J. A. Justiniano, I. P. McCulloch, and U. Schollwöck, "Spectral functions and time evolution from the chebyshev recursion," *Phys. Rev. B*, vol. 91, p. 115144, Mar 2015.

[40] A. Bastin, C. Lewiner, O. Betbedermatibet, and P. Nozieres, "Quantum oscillations of the hall effect of a fermion gas with random impurity scattering," *Journal of Physics and Chemistry of Solids*, vol. 32, pp. 1811–1824, Jan. 1971.

[41] V. Y. Tsaran and S. G. Sharapov, "Magnetic oscillations of the anomalous hall conductivity," *Phys. Rev. B*, vol. 93, p. 075430, Feb 2016.

[42] Y. F. Suprunenko, E. V. Gorbar, V. M. Loktev, and S. G. Sharapov, "Effect of next-nearest-neighbor hopping on the electronic properties of graphene," *Low Temperature Physics*, vol. 34, no. 10, pp. 812–817, 2008.

[43] A. Kretinin, G. L. Yu, R. Jalil, Y. Cao, F. Withers, A. Mishchenko, M. I. Katsnelson, K. S. Novoselov, A. K. Geim, and F. Guinea, "Quantum capacitance measurements of electron-hole asymmetry and next-nearest-neighbor hopping in graphene," *Phys. Rev. B*, vol. 88, p. 165427, Oct 2013.

[44] A. Ferreira, J. Viana-Gomes, Y. V. Bludov, V. Pereira, N. M. R. Peres, and A. H. Castro Neto, "Faraday effect in graphene enclosed in an optical cavity and the equation of motion method for the study of magneto-optical transport in solids," *Phys. Rev. B*, vol. 84, p. 235410, Dec 2011.

[45] H. Shirkani, F. Amiri, and M. Golshan, "Effects of external magnetic fields and rashba spin-orbit coupling on spin conductance in graphene," *Superlattices and Microstructures*, vol. 64, pp. 418 – 426, 2013.